CHARACTERIZATION OF ENGLACIAL VOIDS USING RADAR VELOCITY ANISOTROPY

by

Joshua David Nichols

A thesis

submitted in partial fulfillment

of the requirements for the degree of

Master of Science in Geophysics

Boise State University

May 2010

BOISE STATE UNIVERSITY GRADUATE COLLEGE

DEFENSE COMMITTEE AND FINAL READING APPROVALS

of the thesis submitted by

Joshua David Nichols

Thesis Title: Characterization of Englacial Voids Using Radar Velocity Anisotropy

Date of Final Oral Examination: 05 April 2010

The following individuals read and discussed the thesis submitted by student Joshua David Nichols, and they evaluated his presentation and response to questions during the final oral examination. They found that the student passed the final oral examination.

John H. Bradford, Ph.D.	Chair, Supervisory Committee
Kasper van Wijk, Ph.D.	Member, Supervisory Committee
Hans-Peter Marshall, Ph.D.	Member, Supervisory Committee
Joel Harper, Ph.D.	Member, Supervisory Committee

The final reading approval of the thesis was granted by John H. Bradford, Ph.D., Chair of the Supervisory Committee. The thesis was approved for the Graduate College by John R. Pelton, Ph.D., Dean of the Graduate College.

ACKNOWLEDGEMENTS

I would like to thank my advisor, Dr. John Bradford, for all the help and support in completing my thesis. I would also like to that my committee members, Kasper van Wijk, Hans-Peter Marshall, and Joel Harper for their insight and questions that have improved my thesis. I would also like to thank other researchers that have helped me work through the data and provided field work opportunities. This work could not have been possible without the help of many field crew members who were willing to give up weeks at a time to help collect the data. I would like to thank my family and my wife for the support and encouragement they have given me throughout the process. I would also like to thank INRA and the NSF (ARC-0454717) for financial support.

ABSTRACT

Glacial hydrology plays an important role in the motion and melt of glaciers. The transport of water through glacial ice is still poorly understood. Previous studies show that much of the water is stored and routed through planar voids within the glacier. From borehole observations and previous radar surveys, the voids appear to have a preferential orientation. Transverse waves, including radar waves, and shear seismic waves, travel at different velocities when polarized at different orientations relative to aligned inclusions. I conducted two georadar surveys on Bench glacier, in the Chugach Mountains, AK. Bench glacier has been the field site of a collaborative effort to characterize these englacial voids, and their role in glacial hydrology. Since georadar velocity is commonly used to estimate glacial water content, it is important to know the orientation of the voids relative to the georadar polarization, in any estimation of the water content. From mixing models with aligned inclusions, I was able to estimate the degree of velocity anisotropy expected from water filled voids in glacier ice. Surveys over the same area conducted with different polarizations, yielded velocity estimates that were measurably different.

The first survey was conducted in 2006. This was a large multi-offset multi-azimuth 3D survey. The grid was surveyed in three directions to measure the differences in the radar wave velocities due to orientation. This survey not only provided estimates of velocities in over 3000 locations, but also produced a 3D volume showing englacial

structure. The distribution of velocities in each direction was statistically different and showed an anisotropic velocity field that agreed with the theory and previous observations on Bench glacier. The second survey was a common midpoint survey conducted in 2008. This survey was designed to quickly test for and give an estimate of subsurface anisotropy. I collected common midpoint gathers with three different antenna configurations in five different directions. By doing so, I was able to sample the same part of the glacier with waves with different polarizations. Again this survey showed measurable anisotropy with the fastest velocity occurring when the wave was polarized perpendicular to the long axis of the voids.

Both surveys show measurable anisotropy greater than the uncertainty in the velocity estimates. If preferentially aligned inclusions are suspected, it is necessary to assume an anisotropic velocity model. By assuming an isotropic velocity model, volumetric water content estimates ranged from 0% to 8%. By assuming an anisotropic model, the water content estimate is better constrained and found to be 1.2%. In this work, I demonstrate how to survey and determine velocity anisotropy resulting from aligned inclusions and the importance of an anisotropic velocity model for estimating water content in temperate glaciers.

TABLE OF CONTENTS

LIST OF TABLES

LIST OF FIGURES

LIST OF VARIABLES

Variable	Meaning	Value/units
c	Speed of light	0.3 m/ns
E	Wavefield	
G	Gravitational acceleration	9.81 m/s^2
i	$\sqrt{-1}$	
k	Wave number	
K	Relative Dielectric Permittivity	
L	Depolarization factor	
P_o	Atmospheric Pressure	101.325 kPa
R	Ideal Gas Constant	8.314 J/K
S	Order parameter	
t	Two way travel time	ns
t_0	Zero offset two way travel time	ns
T_o	Surface temperature	273.15 K
v	Radar wave velocity	m/ns
x	Horizontal distance	m
z	Depth	m
β'	Rate of change of the melting point with pressure	9.8 e-5 K/kPa
ε	Dielectric permittivity	F/m
θ_a	Volumetric air content	
θ_w	Volumetric water content	
ξ	Water concentration	
ρ_i	Density of ice	917 kg/m^3
□	Angle	
ω	Frequency	MHz
Subscripts		
i	Ice	
a	Air	
w	Water	
⊥	Perpendicular	
||	Parallel	
1	Host medium	
2	Inclusions	

CHAPTER 1: INTRODUCTION

The global climate is changing. Ice sheets and glaciers are sensitive indicators of global climate change (O'Neel et al., 2005). This warming is shown by more rapid motion and thinning of outlet glaciers in Greenland (Thomas et al., 2000). Additionally, over the last 50 years, approximately 9% of the total sea level rise was attributed to the melting of Alaskan glaciers (Arendt et al., 2002; Pfeffer et al., 2008; Meier et al., 2007). Of particular importance to glacier and ice sheet studies in a changing climate are their hydrologic systems. However, the hydrology of englacial and subglacial flow is poorly understood. Glacial hydrology is closely linked to the climate, and consequently as the climate warms, the amount, location, and timing of release of the water stored in the glacier will also change. This in turn will alter the geometry of the glacier. Additionally, as the geometry changes, so will the sliding dynamics of the glacier, further changing the storage and release of water.

Geophysical Methods for Glacier Investigation

In the investigation of glaciers and their hydrologic properties scientists have used many different methods including borehole logging, slug tests, down hole pressure transducers, dye tests, global positioning system (GPS) tracking, and geophysical methods. The common geophysical methods used in glaciological studies are remote sensing, seismic, and georadar surveys. Remote sensing surveys commonly use airborne craft or satellites to gather large scale altimeter measurements. From this, the mass and

movement of glaciers and ice sheets can be monitored (Johannessen et al., 2005). Seismic reflection surveys can yield information on the internal structure of glaciers, but due to their relatively low frequency, they are generally used to map the glacier bed (Betterly et al., 2007; Navarro et al., 2005; Benjumea and Teixido, 2001).

The logistical challenges of seismic surveys also limit their use in glacial environments. The most common high resolution geophysical survey is georadar. Georadar has been used since 1929 (using radiointerferometry) to determine the depth of glaciers (Stern, 1929; Olhoeft, 2007). Originally used to measure ice thickness, advances in radar technology and processing techniques now allow scientists to use georadar to investigate internal glacial structures (Petterson et al., 2003; Bradford et al., 2009; Brown et al., 2009).

Murray et al. (2000) surveyed Falljökull with both surface and borehole radar and found that diffractions within the glacier are a result of water filled voids, and the varying concentration of those voids within the glacier can be mapped using georadar. Petterson et al. (2004) used radar to map the spatial variability in water content in temperate ice on Storglaciären. The distribution and orientation of water filled voids in a polythermal glacier were mapped using georadar, and found to lie in steeply dipping planes associated with a previous high-pressure water system (Barrett et al., 2008). More recently Endres et al. (2009) use congruent radar and seismic velocities to estimate water content and effective medium theory to obtain consistent estimates from both methods. Murray et al. (2007) and Barrett et al. (2007) take closer looks at how errors in the georadar velocity model affect the water content estimates and methods to reduce these errors to better constrain the water content.

Site Description

One glacier that has been studied by hydrologists and geoscientists for a number of years is Bench Glacier (Figure 1), a small mountain glacier near Valdez, Alaska (Fudge et al., 2008; Bradford et al., 2009; Brown et al., 2009; Harper et al., 2007). A collaborative group involving University of Montana, University of Wyoming, University of Colorado, and Boise State University has studied Bench Glacier for nine field seasons, starting in 1999. This glacier was chosen for its simple geometry, and proximity to Valdez, Alaska. Bench Glacier is approximately 1 km wide and 8 km long. Other than an ice fall that separates the accumulation zone from the ablation zone, the glacier has a fairly shallow slope ~10°. The glacier thickness averages about 180 m, and it has a "hard bed". A "hard bed" means widespread till is not present at the bed of the glacier. Since the beginning of research on Bench Glacier, this group has monitored pressure changes in over 20 boreholes, recorded outlet stream flow, measured glacier movement using GPS and seismographs, along with performing many other hydrologic and geophysical surveys (Bradford et al., 2009; Meierbachtol et al., 2008; Fudge et al., 2008; Brown et al., 2009; Harper et al., 2005). The surveys have ranged from instant measurements to time lapse measurements spanning multiple years. Figure 2 shows locations of geophysical surveys conducted on Bench Glacier between 1999 and 2009. Bench Glacier provides a well-characterized field site and a simple geometry for further investigation of glacial hydrology.

Figure 1 Photograph of Bench Glacier

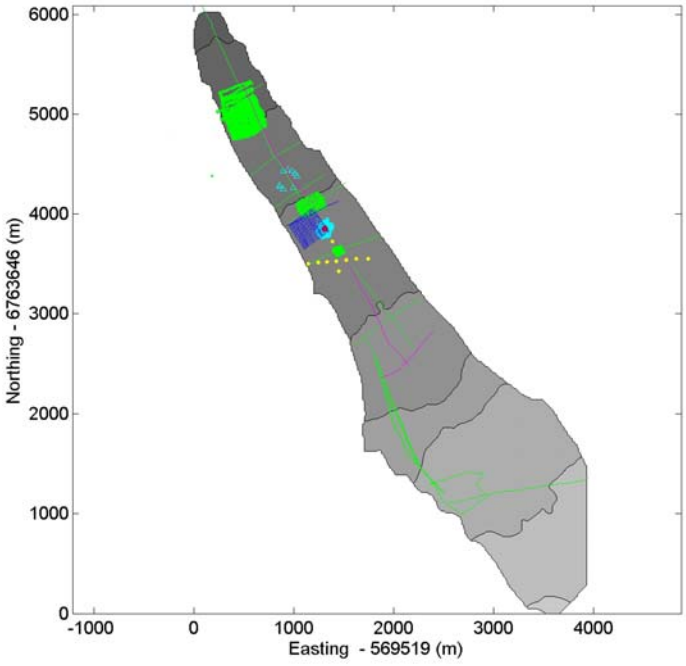

Figure 2 Geophysical investigations on Bench Glacier. Green represents common offset georadar surveys. Light blue: multi-offset multi-azimuth georadar surveys, dark blue: 3D seismic survey, yellow: passive seismic monitoring, red: borehole radar.

Englacial Voids

There are three types of glaciers; polar, temperate, and polythermal. Polar glaciers are located at high altitude and/or high latitudes. The ice within a polar glacier is below the pressure melting point, and therefore has no unfrozen water inclusions. The ice in temperate glaciers is at the pressure melting point, and there are inclusions of unfrozen water within the ice. Polythermal glaciers have a layer of polar ice over top of a layer of temperate ice. There is a distinct boundary observed in radargrams, where the upper (polar) ice appears as radar transparent, and the lower section (temperate ice) is filled with diffractions caused by the water inclusions (Patterson, 1994). Brown et al. (2009) show a distribution of radar scattering events similar to other glaciers (Arcone and Yankielun, 2000; Jacobel and Raymond, 1984). In temperate glaciers and in zones of temperate ice within polythermal glaciers these scattering events are typically attributed to concentrations of unfrozen water. Fountain and Walder (1998) hypothesize that englacial hydrology is dominated by a network of crevasses joined by horizontal conduits. Fountain and Walder (1998) also hypothesize that these conduits have cylindrical bases, shaped by flowing water. Harper and Bradford (personal communication, 2008) theorize that the majority of radar scatterers are planar not cylindrical. Their hypothesis is supported by borehole video of many voids (McGee et al., 2003). Figure 3 shows images from these recordings, which show the voids as planar. These water filled vacancies are termed “planar voids” to describe the shape without implying a mechanism. The voids are most prominent below a radar transparent zone, which extends from the surface to 20 m deep on average (Brown et al., 2009). Further investigation is required to determine the cause of the transparent layer. Similar voids are

also observed in studies by Fountain et al. (2005). Fudge et al. (2008) drilled over 50 boreholes, and monitored water levels in the holes on Bench Glacier to better understand the relationship of the void system to the glacial hydrology. The boreholes were drilled with a hot water high pressure drill to various depths, often intersecting voids. They performed slug tests by adding water to one borehole and monitoring water depth and pressure changes in adjacent boreholes. Some slugs produced little to no response in adjacent boreholes. Slug tests in other boreholes, did show a change in pressure. Some of these boreholes were not connected to the bed of the glacier (Meierbachtol et al., 2008). From this they hypothesized that voids can be connected to other voids, the glacier bed, or isolated. The voids also appear to have a preferential orientation, based on compass recordings in the borehole video (Harper et al., 2008). The observed orientations are shown in Figure 4. Bench Glacier was also surveyed using georadar to image these voids (Bradford et al., 2009; Brown et al., 2009; Bradford and Harper, 2005). Bradford (personal communication, 2008) conducted a common offset survey with 50 MHz antennas. This 3D section was processed and migrated to provide a 3D image of the glacier. By stepping through the volume in time, horizontal cross-sections can be viewed as time slices. Time slices of the radar volume show linear events, which are interpreted to be drainage features such as the observed voids (Figure 5). The orientation of these features meshes well with the observed orientation in the borehole video, roughly 45° to the glacier flow.

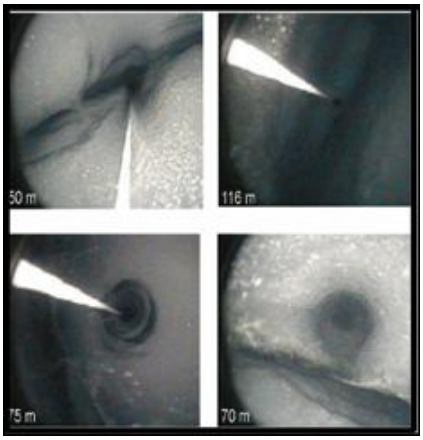

Figure 3 **Borehole video images of planar voids, Bench Glacier, Alaska. The voids ranged in size from a few cm to over a meter.**

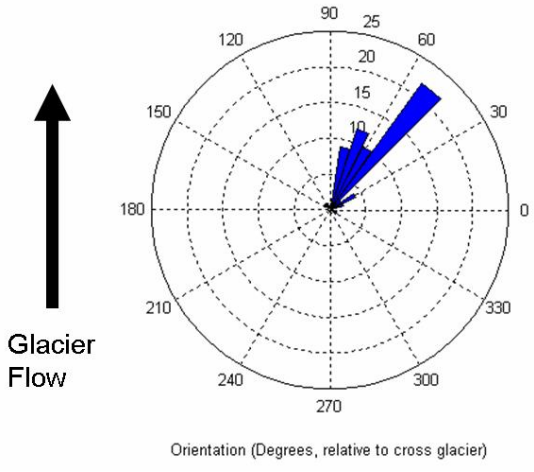

Figure 4 **Fracture directions, measured with compass from boreholes.**

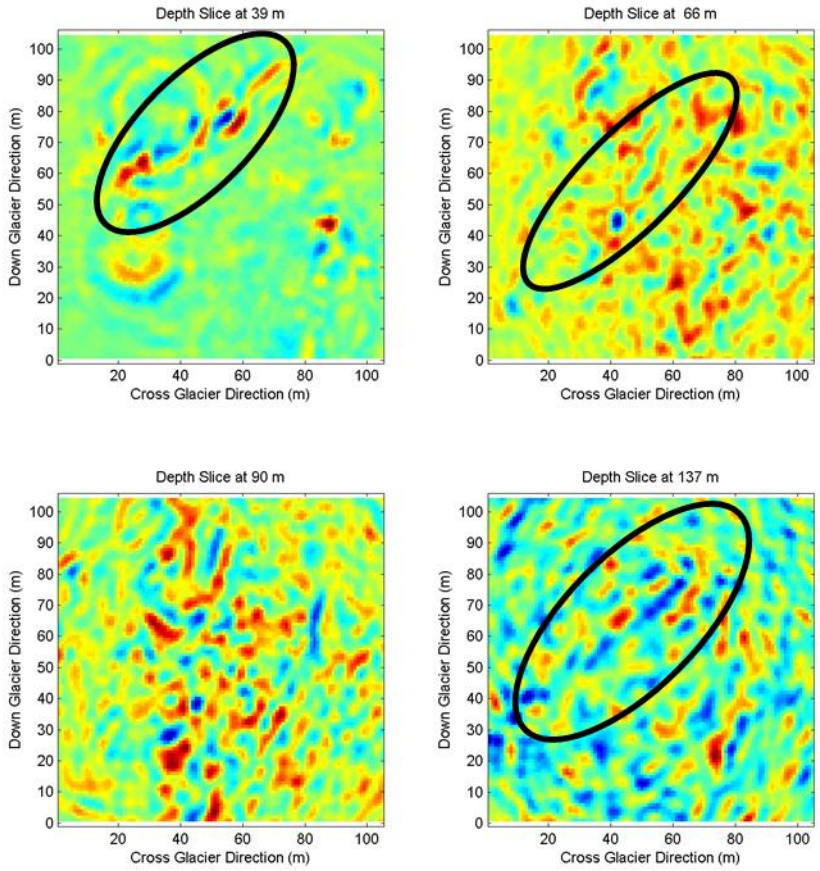

Figure 5 Time slices from common offset survey. (Bradford, personal com., 2008). Note the interconnected linear events that are oriented roughly 45 º to glacier flow.

The voids likely play an important role in the transport of water from the surface to the bed. Understanding this role will help quantify the storage and release of water within the glacier. The orientation of the voids has significant implications for studies using georadar or seismic surveys to estimate water content. Wave propagation will be anisotropic through a medium with aligned fractures or voids (Schoenberg and Sayers, 1995; Shen et al., 2002; Tsvankin and Lynn, 1999). If the velocity field is assumed to be

isotropic, the potential exists for different surveys conducted over the same area to yield different predictions for water content because they were surveyed in different directions.

Chapter Review

Glaciers play an important role in the global water storage system and can yield insights into the workings of larger ice sheets. Understanding the role of these glaciers in global water estimates is important. Georadar is an effective tool to investigate water content of glaciers. Previous studies on Bench Glacier and others show that water is stored in aligned fractures in temperate glaciers. Constraining the water content estimates in temperate glaciers is critical to understanding glacier mass balance and movement as well as estimating sea level rise. While georadar is an effective tool for estimating water content, care must be taken as waves travel at different speeds depending on their polarization to aligned fractures.

CHAPTER TWO: REVIEW OF RADAR METHODS

Georadar was originally used in ice and glacier studies (Bailey et al., 1964), and is now used in many non-destructive near-surface investigations. Some of the more common uses for georadar are investigating concrete and asphalt structures, mapping ground water, and imaging subsurface structures in both ground, and ice (Annan, 2005). When studying a medium using georadar, an electromagnetic field propagates through the medium as a wave. The wave is scattered, or reflected, by dielectric permittivity changes in the subsurface. The scattered energy which returns to the receiving antenna is recorded, and when positioned properly in space and time, the response shows changes in electromagnetic properties. Typical commercially available radar frequencies are between 1 MHz to 1 GHz. In this frequency range the signal can penetrate well, and the fields are not diffusive (Annan, 2005). Also in typical subsurface and non-destructive testing surveys scattering losses due to heterogeneity constrain the upper limit of suitable frequencies. As the frequency increases so does the resolution of the georadar. Vertical resolution is commonly estimated to be about ¼ wavelength; however this is dependent on the pulse width and subsurface material. The lateral resolution typically goes as $\sqrt{\frac{\lambda d}{2}}$. If the data are collected as a 3D survey, migration removes the depth dependency of the resolution. However, lower frequency waves (longer wavelength) can propagate deeper due to lower scattering attenuation. In most subsurface applications at a certain length

scale there is heterogeneity, and the closer the wavelength is to this scale, the more the wave is attenuated (Annan, 2005). In addition to the depth and size of the target reflector, the electric properties of both the surrounding medium and target medium play affect the velocity of the radar wave.

Permittivity and Velocity

One important material property in georadar surveys is the dielectric permittivity, which describes the displacement of constrained charges in the presence an electric field. More specifically, the importance is the relative complex dielectric permittivity K, which is the ratio of the permittivity of the medium to that of free space. The propagation velocity of radar, v, is related to the relative dielectric permittivity, by equation 1:

$$\sqrt{K} = {}^{c}\!/_{v}, \qquad (1)$$

where c is the speed of light in free space. Table 1 shows typical relative permittivities, and velocities for common materials.

Table 1 Relative permittivity and velocity for common materials. Adapted from Annan (2005).

Material	K (relative permittivity)	v (m/ns)
Air	1	0.30
Water	87	0.033
Ice	3-4	0.168
Granite	4-6	0.13
Shales	5-15	0.09
Dry Sand	3-5	0.15
Saturated Sand	20-30	0.06

Due to the difference in radar velocity traveling through water (0.033 m/ns) and through glacier ice (0.168 m/ns), velocity is commonly used to estimate water content in glaciers (Murray et al., 2007; Petterson et al., 2004). Variations in ice velocity are commonly associated with changes in air and water content. Normal moveout (NMO) radar velocities are commonly estimated by the common midpoint (CMP) method (Yilmaz, 2001). An alternative approach to determining radar velocities is migration velocity analysis (MVA) (Bradford and Harper, 2005). The effective relative permittivity can be related to the volumetric water content (θ_w) using a mixing formula such as the CRIM (Complex Refractive Index Method) equation (Wharton et al., 1980):

$$\theta_w = \frac{\sqrt{K} - \sqrt{K_i} - \theta_a\left(\sqrt{K_a} - \sqrt{K_i}\right)}{\sqrt{K_w} - \sqrt{K_i}}, \qquad (2)$$

where θ_a is volumetric air content, K_a (1), K_i (~3.2), and K_w (~87) are the relative dielectric permittivities of air, dry solid ice and water respectively. Bradford et al. (2009) calculate the depth dependent volumetric air content by summing discrete volume elements:

$$\theta_{a(k+1)} = \frac{RT_0}{\left[G\rho_i \Delta z \sum_{k=1}^{n}\left(1 - \theta_{a(k)}\right)\right] + P_0} - R\beta', \qquad (3)$$

where R is the gas constant, T_0=273.15, G is gravitational acceleration, ρ_i is the density of ice (0.917g cm^{-3}), P_0 is the atmospheric pressure, Δz is the depth step, and β' is the rate of change of the melting point with pressure for air saturated water. This equation only accounts for hydrostatic pressure, and does not account for changes related to longitudinal stress. Equation 3 should not be applied to ice sheets, as the ideal gas law does not apply to pressures found deep in the ice sheet. Inserting equation 3 into

equation 2 creates a depth dependent mixing model. Both Bradford and Harper (2005) and West et al. (2007) estimate the air bubble concentration may be as much as 16 % in the upper layers. Assuming θ_a =0.1 at the surface of the glacier, the volumetric air concentration at depth can be calculated using equation 3 as shown in Figure 6.

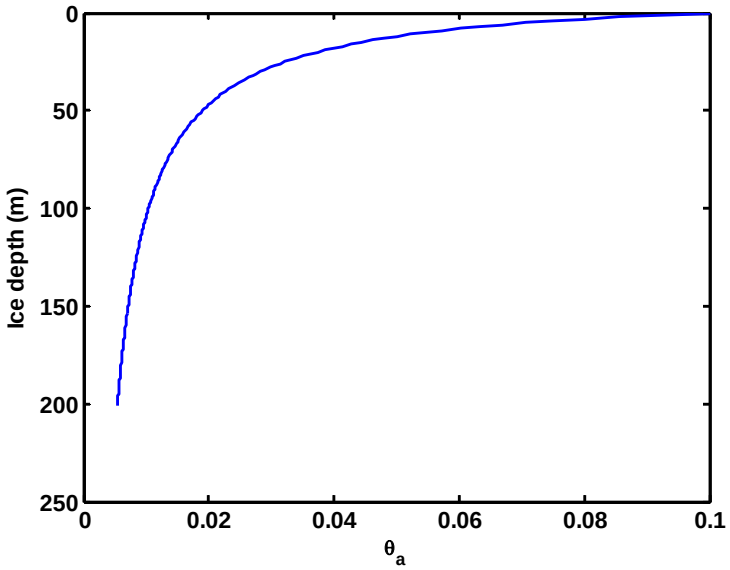

Figure 6 Vertical distribution of air volume vs. ice depth. Calculated using equations 2 and 3.

From Figure 6 and equation 3, the air content is less than 2% below 50 m depth. Inferring that the air content in bubbles is constrained by the pressure at depth, it follows that the voids would follow the same trend. The deeper the voids are in the glacier the less likely it is that air could keep the void open due to the pressure at that depth, unless stresses caused by irregular bed geometry were present. The voids below the transparent layer are therefore likely filled with water. This hypothesis agrees well with radar velocities and borehole observations (Bradford et al., 2009; Brown et al., 2009).

Fracture Dependent Anisotropy

Fractures that have a preferred orientation have been shown to induce anisotropic velocity in seismic surveys (Schoenberg and Sayers, 1995; Shen et al., 2002; Tsvankin and Lynn, 1999). Studies looking at the brine concentration of sea ice show attenuation anisotropy in radar waves (Kovacs & Morey, 1978). Other studies show anisotropic reflection amplitude and phase responses (Van Gestel & Stoffa, 2001; Sassen & Everett, 2009; Tsoflias et al., 2004). Matsuoka et al. (2003) investigated the effect the ice fabric, known to be anisotropic, has on different polarization of radar waves in Antarctica. The anisotropy of englacial water storage is shown to have an effect in both lab experiments as well as on Mýrdalsjökull glacier (Matsuoka et al., 2007). Anisotropic radar responses relating to inclusions within glaciers have been observed since 1999 (Nobes, 1999). Nobes (1999) hypothesized that the magnitude and coherence of the radar signal are azimuthally dependent on oriented structures at depth. Scatterers were found to be oriented consistently in planes oriented cross glacier using multiple polarizations of radar waves by Barrett et al. (2008).

Aligned fractures should also induce velocity anisotropy. Seismic waves polarized perpendicular to the orientation of the fractures travel slower than those polarized parallel to the fractures. For radar waves, the opposite should be true, based on the application of Ampère's Law. Figure 7 shows an idealized georadar wavefront approaching a water filled inclusion, where red is positive and black is negative on the dipoles within the inclusion. In Figure 7A the electric field of the radar wave is polarized parallel to the long axis of the inclusions, and the dipoles bound at the interface must rotate more to align to the field, slowing down the wave. If the radar wave is polarized

perpendicular to the long axis of the inclusions, there are fewer dipoles at the interface that need to align with the field, and the wave travels faster (Figure 7B). Radar waves should travel fastest when polarized perpendicular to the fractures and slowest when parallel as in Figure 8 (red is the fast direction and green is the slow direction).

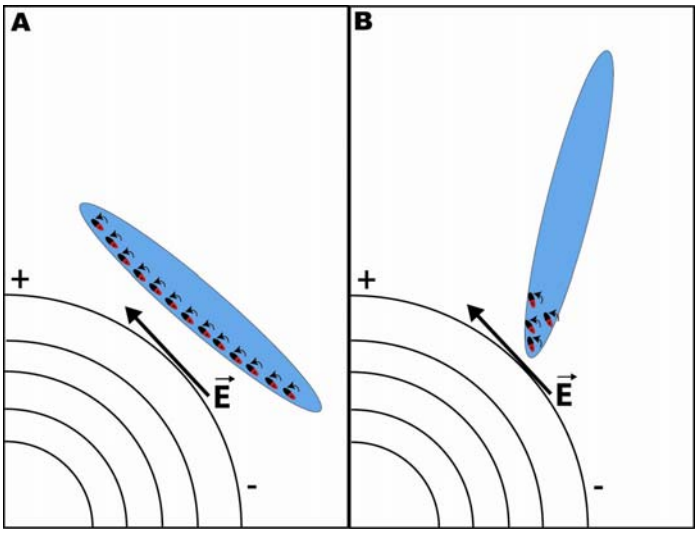

Figure 7 **Cartoon illustrating a wave front polarized parallel (A) and perpendicular (B) to the long axis of the inclusion.**

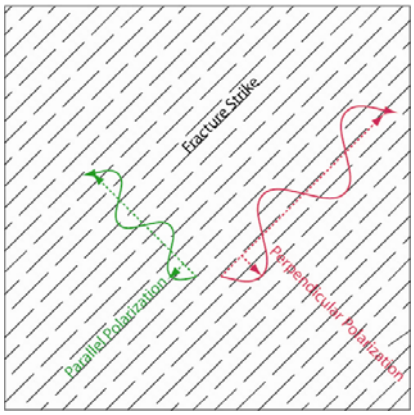

Figure 8 **Cartoon showing fast and slow directions due to fracture induced velocity anisotropy.**

Taylor (1965) presents three equations which describe the effective dielectric permittivity for a mixture of perfectly aligned ellipsoidal bodies (spheres, needles and disks) (Figure 9) in an electric field, where ξ is the volumetric concentration of the inclusions, ε_1 and ε_2 are the permittivities of the host medium, and inclusions respectively, ε is the effective dielectric permittivity of the mixture:

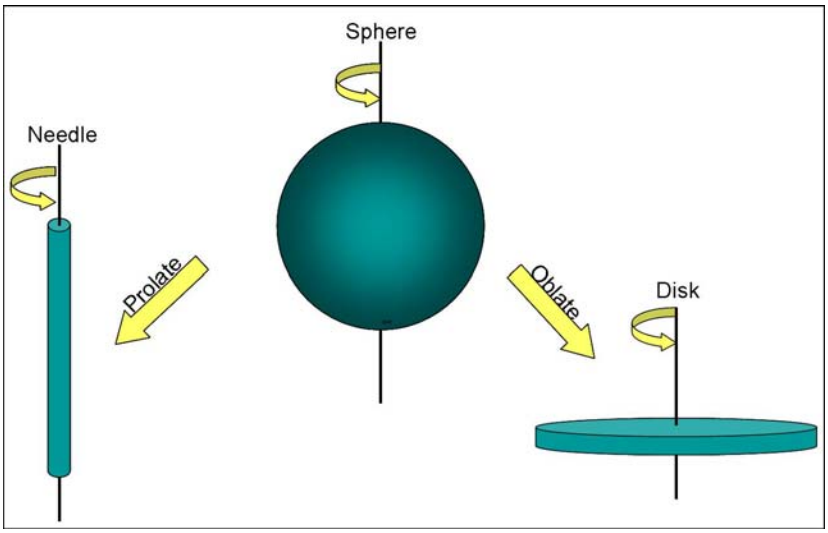

Figure 9 Diagram of ellipsoidal bodies; a sphere, a needle, and a disk. The needle and disk are formed by stretching along either the axis of rotation (needle) or the perpendicular axes (disk)

1) Disks with Major Axis Parallel (Needles with Major Axis Perpendicular) to the field

$$\varepsilon/\varepsilon_1 = 1 - \xi\left(1 - \left(\varepsilon_2/\varepsilon_1\right)\right) \tag{4}$$

2) Needles with Major Axis Parallel to the field

$$\varepsilon/\varepsilon_1 = 1 - 2\xi\left(1 - \left(\varepsilon_2/\varepsilon_1\right)\right)\frac{\left(\varepsilon/\varepsilon_1\right)}{\left(\varepsilon/\varepsilon_1\right) + \left(\varepsilon_2/\varepsilon_1\right)} \tag{5}$$

3) Disks with Major Axis Perpendicular to the Field

$$\varepsilon/\varepsilon_1 = 1 - \xi\left(1 - \left(\varepsilon_2/\varepsilon_1\right)\right)\frac{\left(\varepsilon/\varepsilon_1\right)}{\varepsilon_2/\varepsilon_1} \tag{6}$$

In addition, Taylor (1965) calculates the effective permittivity for spheres, as well as randomly oriented needles and disks. Figure 10 shows the effective radar velocity vs. the percent volume of inclusions, for different types, and polarization of the wave relative to the inclusions (Taylor, 1965).

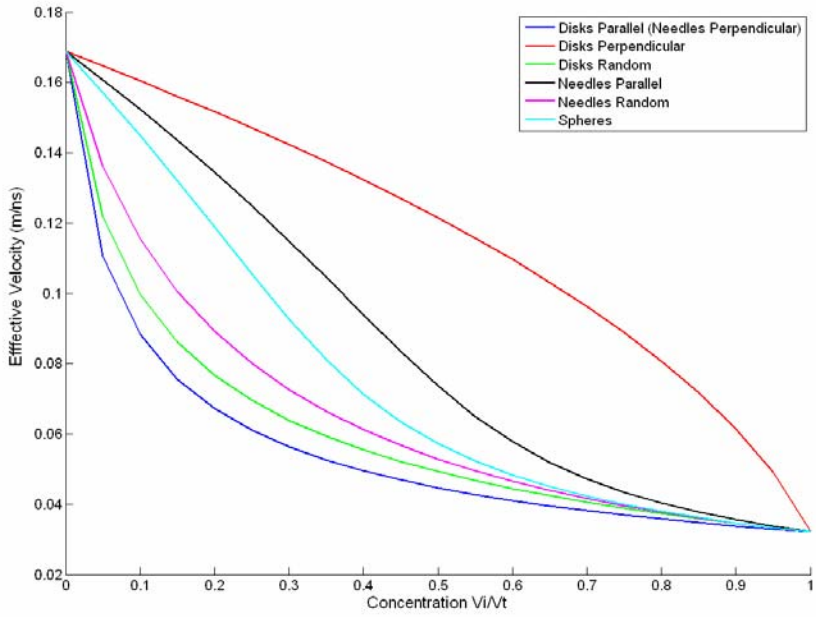

Figure 10 Radar velocities for water filled inclusions in ice. Inclusion orientation is the axis of rotation relative to polarization of the wave.

From Figure 10 it is clear that the apparent velocity is heavily dependant on not only the concentration but also the shape and orientation of the inclusions. The greatest difference in velocity is between disks oriented parallel and perpendicular to the polarization of the wave. It seems unlikely that inclusions would naturally be perfectly aligned. A more general equation to determine the effective permittivity tensor that includes both the shape and the degree of order of the inclusions is given by Giordano (2005):

$$1-\xi=\frac{\varepsilon_2-\varepsilon_\perp}{\varepsilon_2-\varepsilon_1}\left(\frac{\varepsilon_1}{\varepsilon_\perp}\right)^{\frac{3L(1-2L)}{2-3L+S-3SL}}\times\left[\frac{(1+3L-S+3SL)\varepsilon_1+(2-3L+S-3SL)\varepsilon_2}{(1+3L-S+3SL)\varepsilon_\perp+(2-3L+S-3SL)\varepsilon_2}\right]^{\frac{(1-3L)^2(2+S)(1-S)}{(2-3L+S-3SL)(1+3L-S+3SL)}}$$

$$1-\xi=\frac{\varepsilon_2-\varepsilon_\parallel}{\varepsilon_2-\varepsilon_1}\left(\frac{\varepsilon_1}{\varepsilon_\parallel}\right)^{\frac{3L(1-2L)}{2-3L-2S+6SL}}\times\left[\frac{(1+3L+2S-6SL)\varepsilon_1+(2-3L-2S+6SL)\varepsilon_2}{(1+3L+2S-6SL)\varepsilon_\parallel+(2-3L-2S+6SL)\varepsilon_2}\right]^{\frac{2(1-3L)^2(2+S)(1-S)}{(2-3L-2S+6SL)(1+3L+2S-6SL)}}$$

, (7)

where, ξ is the concentration, ε_1 and ε_2, are the permittivities of the host medium and inclusions, and $\varepsilon_\parallel$ and $\varepsilon_\perp$ are the effective permittivities measured parallel and perpendicular to the rotational axis of the inclusions. S is a parameter describing the state of order of the inclusions based on a statistical distribution of the orientations of the inclusions. The state of order varies from S=0 (perfectly random) to S=1 (perfect order). The shape of the inclusions is represented by the depolarization factor L in equation 7. The spheroids can vary from needle shaped (L=1/2), to spheres (L=1/3), to penny shaped disks (L=0). Since the englacial voids in Bench glacier appear to be planar, I represent them as lamellae, or disks. Giordano (2005) also accounts for the state of order, or how well the spheroids' axes of rotation are aligned. If we represent the planar voids as disks (L=0) equation 7 can be solved explicitly for the effective permittivity parallel ($\varepsilon_\parallel$) and perpendicular ($\varepsilon_\perp$) to the average axis of rotation (minor axis):

$$\varepsilon_\parallel=\frac{(1-S)\varepsilon_1\varepsilon_2+(S+2)\left(\varepsilon_1\varepsilon_2+\xi\varepsilon_2{}^2-\xi\varepsilon_1\varepsilon_2\right)}{(1-S)\left(\varepsilon_2(1-\xi)+\xi\varepsilon_1\right)+(2+S)\varepsilon_2}$$

$$\varepsilon_\perp=\frac{(1+2S)\varepsilon_1\varepsilon_2+(2-2S)\left(\varepsilon_1\varepsilon_2+\xi\varepsilon_2{}^2-\xi\varepsilon_1\varepsilon_2\right)}{(1+2S)\left(\varepsilon_2(1-\xi)+\xi\varepsilon_1\right)+(2-2S)\varepsilon_2}\quad , \tag{8}$$

To approximate the order of the englacial voids, consider Figure 4. This shows the fracture orientation for all fractures to be within 15° from the mean direction. The order S can be found by solving this integral, where f (□) is the probability distribution function representing the orientation of the voids:

$$S = \int_0^{\pi} \left(\frac{3}{2}\cos^2(\phi) - \frac{1}{2} \right) f(\phi) d\phi \qquad (9)$$

For a mean angle of 0º with decreasing probability to 15º on either side the function is represented by a cosine (Figure 11):

$$f(\phi) = \begin{cases} \cos(6\phi) & 0 \le \phi \le \dfrac{\pi}{12} \\ 0 & \dfrac{\pi}{12} < \phi \le \pi \end{cases} \qquad (10)$$

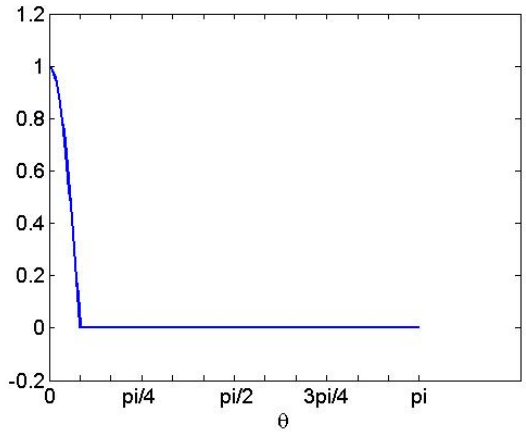

Figure 11 Distribution function for angle of inclusions

From equations 9 and 10, S=0.9 for inclusions with an axis of rotation that varies less than 15° from the mean. Figure 12 shows the effective velocity vs. percent volume of disks for different states of order, including S=0. 9. The host velocity is calculated from the depth dependant mixing model, with θ_w set to zero. Only appropriate velocities and concentrations for water filled inclusions in glacier ice are shown. The effect of the inclusions on the velocity anisotropy is greater when the inclusions are more ordered.

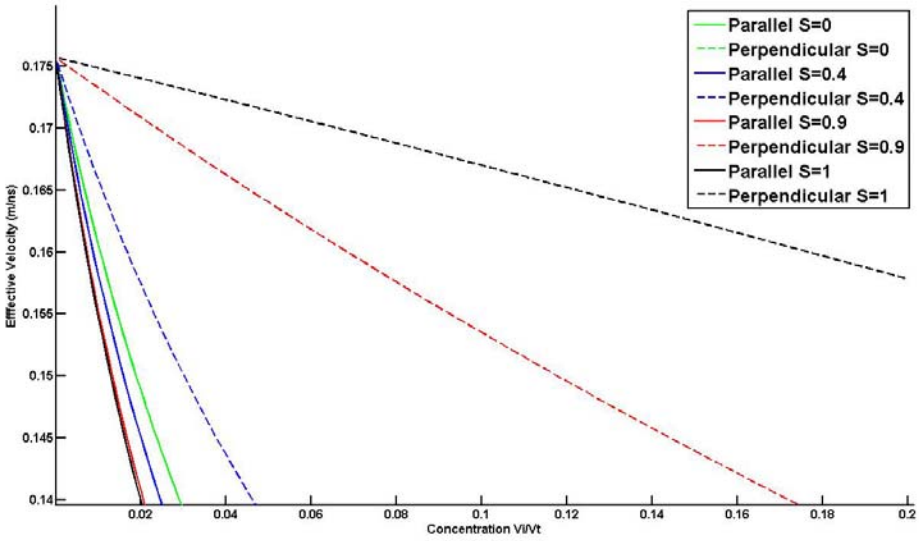

Figure 12 Radar velocities for water filled disks in ice. The velocity contrast between the parallel and perpendicular orientation increases as the disks become more aligned.

Data Collection

Typical georadar surveys involve a single transmitter and one receiver. These are positioned a common distance apart and moved along a line over the survey area. This acquisition method is called common offset (Figure 13). This provides a representation of the cross-section of the subsurface, showing where changes in permittivity are located.

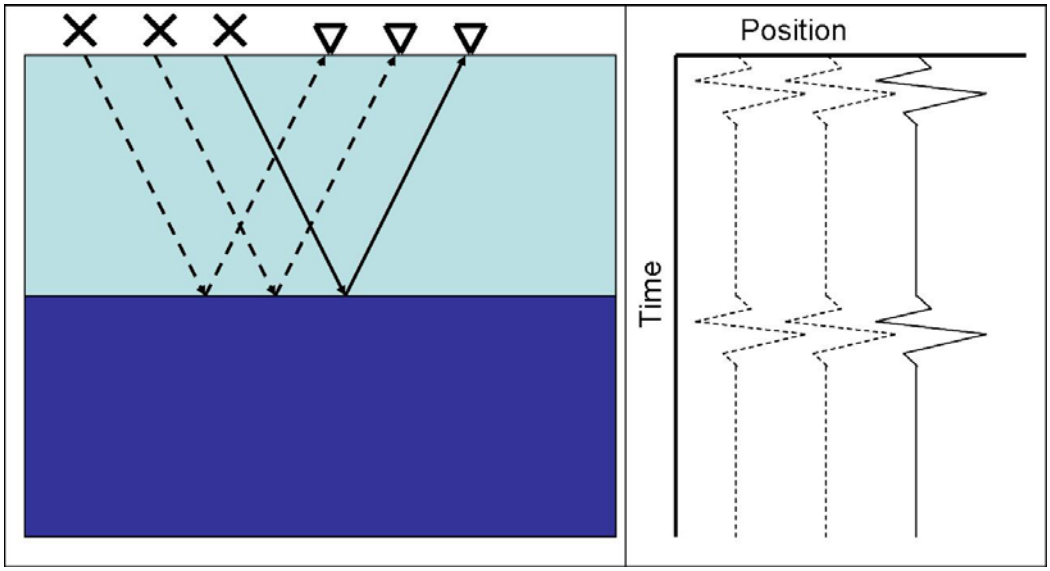

Figure 13 Model of a common offset survey with recorded signal.

The velocity of the radar wave in the material must be known to determine the depth of the permittivity boundaries. The most common method of determining radar wave velocity is the normal moveout (NMO) velocity analysis. As the source and receiver are moved apart centered over a common midpoint the signal reflected from the interface arrives later in time. By fitting a hyperbola to the moveout of the reflection, the mean velocity of the wave traveling above the interface can be determined (Figure 14). The NMO analysis assumes that the velocity difference between layers is small, and reflectors are flat-lying and planar. It is also assumed that the maximum offset to depth ratio is small.

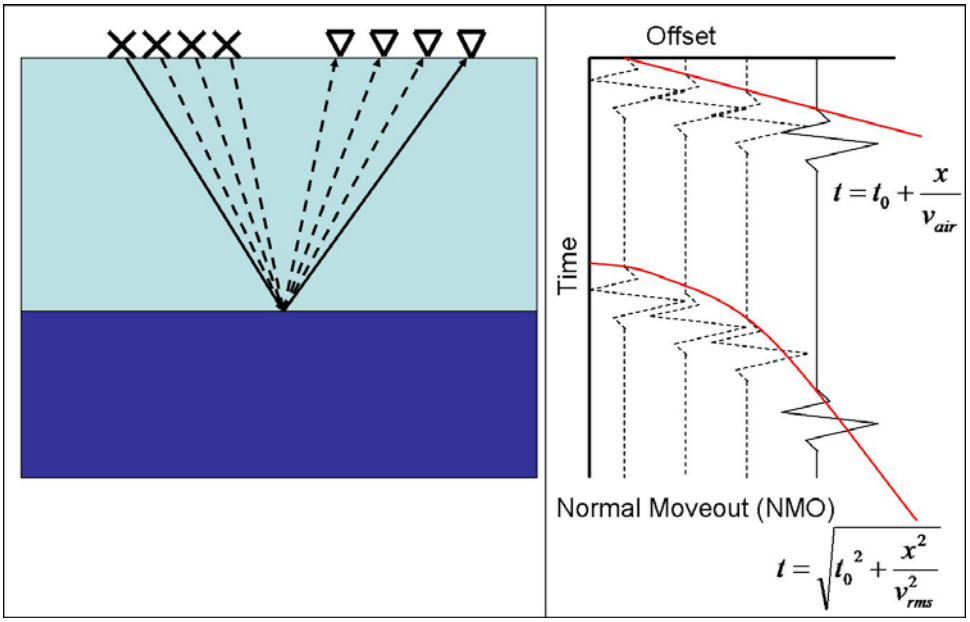

Figure 14 Model of a common midpoint gather and NMO equation.

To better constrain the structure of the subsurface, multiple 2D lines can be collected near each other. Doing so provides a three dimensional representation of the subsurface. This also helps to account for reflections not located directly beneath the survey line, called out of plane reflectors. Advances in georadar technology now allow multiple transmitters and receivers to function at one time. This allows multiple offsets to be collected at once, greatly simplifying the acquisition and providing denser data sampling, however care must be taken in the analysis, as the multiple offsets measured simultaneously do not have the same midpoint.

Data Processing

Preprocessing

After acquiring the data, the locations of the transmitter and receiver need to be assigned to each trace. Depending on the survey design this can either be an absolute position such as UTM coordinates, or a relative position such as meters from the

beginning of the survey line. This step is crucial to the utility of the data. Without an accurate location of both the transmitter and the receiver, the midpoint is unknown. Errors in midpoint position can result in an incorrect estimation of the velocity of the wave.

DeWOW

The pulse generated by the transmitter contains a DC component caused by the initial pulse which decays slowly resulting in a low-frequency trend. If not removed this can distort the frequency content of the signal as well as skew the mean amplitude from zero (Jol, 2009).

Time-zero Correction

Once all the traces have positions and have been deWOWed, a time-zero correction is applied. The time-zero correction accounts for electronic drift, fiber-optic cable length, and variations in the air-gap between antennas. These time shifts are corrected for by selecting the first arrival of the air-wave for each trace and shifting the picks to a common time (Jol, 2009).

Filtering and Gaining

In order to emphasize the features most important to the survey, a combination of filters and gains can be employed. By selecting the correct antennas, the frequency content of the data can be limited. A bandpass filter can further restrict the frequencies in the data to those that fall in a narrower range (Yilmaz, 2001). By removing the high frequency signals, the smaller scale heterogeneities and high frequency noise are masked, resulting in a more coherent signal. After filtering the data to a bandwidth containing the

dominant frequency, the data can be gained. Gaining is a process where the amplitude of the recorded signal is either increased or decreased to highlight different parts of the time record. Most commonly gains are applied to boost the amplitude later in time, to compensate for energy lost due to attenuation, and spreading of the wave. Typical gains are the Automatic Gain Control (AGC), and the True Amplitude Recovery (TAR). The AGC works by sampling the amplitudes in a specified time window and taking the average. Then the trailing, leading or center time of the window is corrected using a ratio of the actual amplitude to the average in the window (Yilmaz, 2001). The TAR applies a time variant gain, by multiplying the signal by a function that is time dependant. One function that is used to account for geometric spreading and attenuation is $g(t)= t^2$, where g is the gaining function and t is the two-way travel time (TWTT) (Yilmaz, 2001).

Velocity Analysis

To constrain the velocity of subsurface materials multiple offset data should be collected. To perform an NMO velocity analysis the data need to be sorted into common midpoint gathers. By combining all the traces with the same midpoint and sorting them by increasing offset, the reflected wave from the interface arrives later in time. The difference in time between the zero-offset trace and larger offset traces is called moveout, and can be approximated by equation 11, where t is the TWTT, t_0 is the TWTT at zero offset, x is the offset(distance between source and receiver), and v_{rms} is the root-mean-squared (RMS) velocity of the radar wave above the interface.

$$t^2 = t_0^2 + \frac{x^2}{v_{rms}^2} \qquad (11)$$

A group of traces with the same midpoint is called a common midpoint gather or CMP. The coherency of the signal is calculated and plotted on a velocity vs. zero-offset TWTT graph. The velocity that has the most coherent signal or flattens the moveout the best at that travel time is the RMS velocity. Another method of finding the RMS velocity using the NMO equation is to plot the TWTT to the interface in x^2-t^2 space. The slope of a line fit to the points is $1/v^2$. In this work I treat the entire glacier thickness as one layer, as I am only concerned with the average velocity to the glacier bed. Once the velocity is known, the dielectric permittivity of the material can be determined and the material above the reflector constrained. By knowing the TWTT and the velocity, the depth to the interface can be estimated.

Stacking and Migration

Stacking is the process of averaging the velocity corrected traces in each gather. This increases the signal to noise ratio and produces a more coherent trace. By aligning the stacked traces by position, a stacked section is created. To get a better image of the subsurface, and place the signal response in the correct position either in time or depth, the data must be migrated. In the simplest sense migration collapses diffractions to a point and moves dipping reflectors to their correct angle and position. Migration increases spatial resolution and provides an image of the subsurface. One common migration method for a one-layer velocity model is the phase-shift migration (Gazdag, 1978). A phase-shift migration involves taking a 2D Fourier transform of the stacked section into the frequency-wavenumber (f-k) domain. Then for each frequency (ω), equation 12 is extrapolating downward in depth (z) (Yilmaz, 2001). Extrapolating the wavefield to the maximum depth of the section produces a migrated section in the E (k_x,

z, t=0) space. To get the migrated section in the E(x, z, t=0) space, an inverse transform in the x direction is needed. This is commonly accomplished using a commercial algorithm.

$$E(k_x, z + \Delta z, \omega) = E(k_x, z, \omega)\exp(-ik_z \Delta z) \quad (12)$$

Chapter Review

Georadar is a non-destructive tool used to investigate the electric properties of the subsurface. Recent advances have made georadar more practical for not only getting an image of the subsurface but also constraining the materials and their properties. Since the electrical properties of water are unlike the properties of ice, georadar is well suited for surveys to detect water within glaciers. One potential use of this is using radar velocity anisotropy to detect aligned water filled fractures.

CHAPTER THREE: DATA COLLECTION AND PROCESSING

3D Survey Design and Collection

I performed two georadar surveys on Bench Glacier to more closely examine anisotropy in radar wave velocity due to preferentially aligned inclusions: 1) a 3D survey with multiple offsets and multiple azimuths in 2006 and 1) a multi-azimuthal CMP survey in 2008. The 3D survey provided a 3D image of the study area. By collecting the data with multiple offsets, the velocity of the wave that traveled through the glacier can be established. The 3D survey, conducted in Spring 2006, had a target size of 100 m x 100 m. Using 25 MHz antennas we collected data over 5 days with 15 different offsets ranging from 5 m to 150 m. The survey used a Systems & Software 1000V Pulse transmitter towed approximately 5 m behind a snowmobile. Three receiving antennas were attached to the snowmobile in such a way that their offset from the transmitter could be easily adjusted. Each antenna was supported by three snow sleds connected by PVC tubing. These groups of sleds were then tied together. In addition to keeping the antennas parallel, a skier held tension on the rope and checked equipment status (Figure 15). Two geodetic grade Trimble GPS Receivers were positioned in the center sled of both the transmitting and center receiving antenna. The clock in the georadar was synchronized to the GPS clock at the beginning of each acquisition period so that the trace positions could be interpolated in time. Using this setup we were able to collect data at 11-13 km/hr. The georadar data were collected in three azimuths—0º, 45º, and 90º relative to glacier

flow—in order to detect any anisotropy due to the orientation of the voids. We maintained 4 m spacing between profiles in each azimuthal orientation to better quantify the size and distribution of the voids.

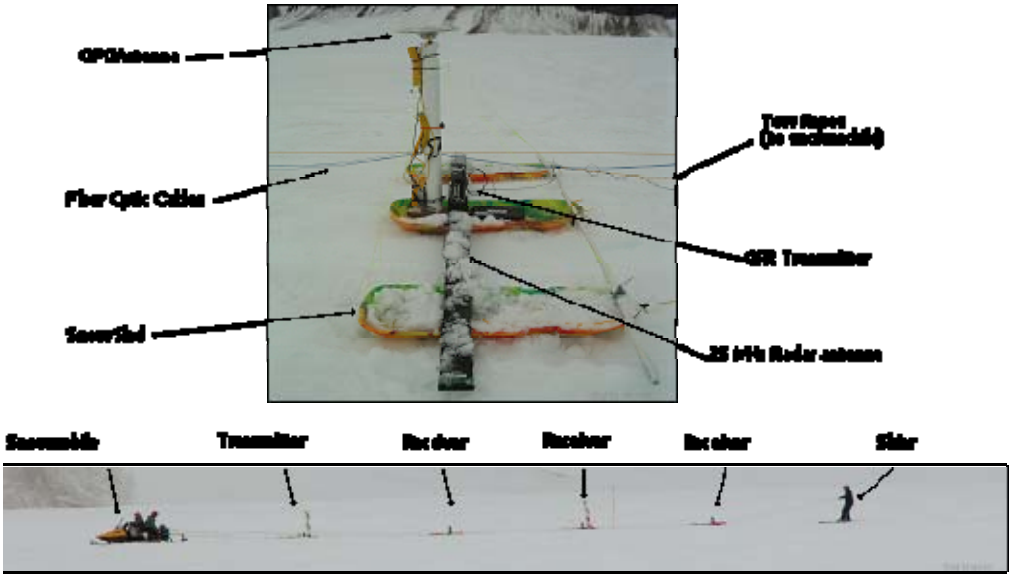

Figure 15 Georadar setup for Multi channel acquisition.

3D Data Processing

Preprocessing

The greatest challenge with the data from the 3D survey was assigning the geometry. Without an accurate geometry, the velocity cannot be determined. The GPS locations for both the transmitter and receiver were split into sections of continuous GPS acquisition. Due to drift in the georadar clock the trace times had to be shifted to correspond with the times the GPS was acquiring positions. The positions for each section were then interpolated using MATLAB to find the locations of the transmitter and

receiver for each trace. For sections where only the GPS on the transmitter or receiver were functioning, the positions were extrapolated based on the path of the working GPS. The midpoint of each trace was then calculated along with the true offset between the transmitter and receiver. All the midpoints that fell within the 100 m grid were sorted into 2 m x 2 m bins. The common depth point (CDP) fold, or number of traces in each bin, was sufficient to extend this to a 110 m grid, allowing for 55 bins in each direction. This resulted in 3025 bins (Figure 16). The average number of traces per bin was 23.3 with a standard deviation of 7.7. On average there were 8 traces per bin for each direction.

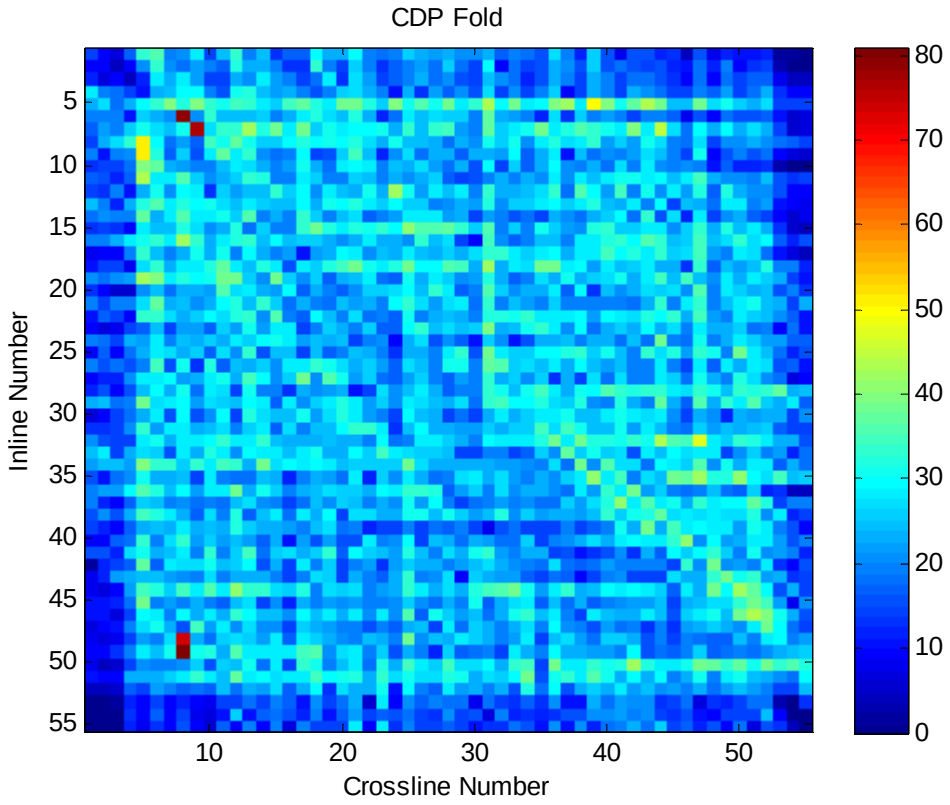

Figure 16 CDP fold for the 100 m by 100 m grid. Each bin is 2m square.

I processed the data using ProMAX 3D. There was good coverage of the grid from the 5-90 m offsets. Due to difficulty synchronizing the radar and GPS clocks the positions of the traces have a maximum uncertainty on the order of meters.

Time-zero Correction

After assigning the survey geometry to the traces, I applied a zero-time correction to the data to correct for difference in cable length, electronic drift and recording start time. I picked the first arrival of the airwave for each trace and shifted them to a time corresponding to the moveout associated with the speed of light through air.

Filtering and Gaining

I applied a 2-4-12-25 MHz trapezoidal bandpass filter, where 2, 4, 12, and 25 MHz define the corners of the trapezoid. By applying a fairly low pass filter, I emphasized deeper interfaces and minimized the effect of small scale heterogeneity. I also used a time-variant gain $g(t)=t^2$ to correct for geometric spreading, boosting the amplitude at later times. Next I picked the time of the bed reflection for all the traces within the grid and sorted the traces by azimuth. I then output the bin number, offset, and two-way travel time (TWTT) to the bed for each trace. Figure 17 shows processed CMP gathers, with the TWTT picks in red.

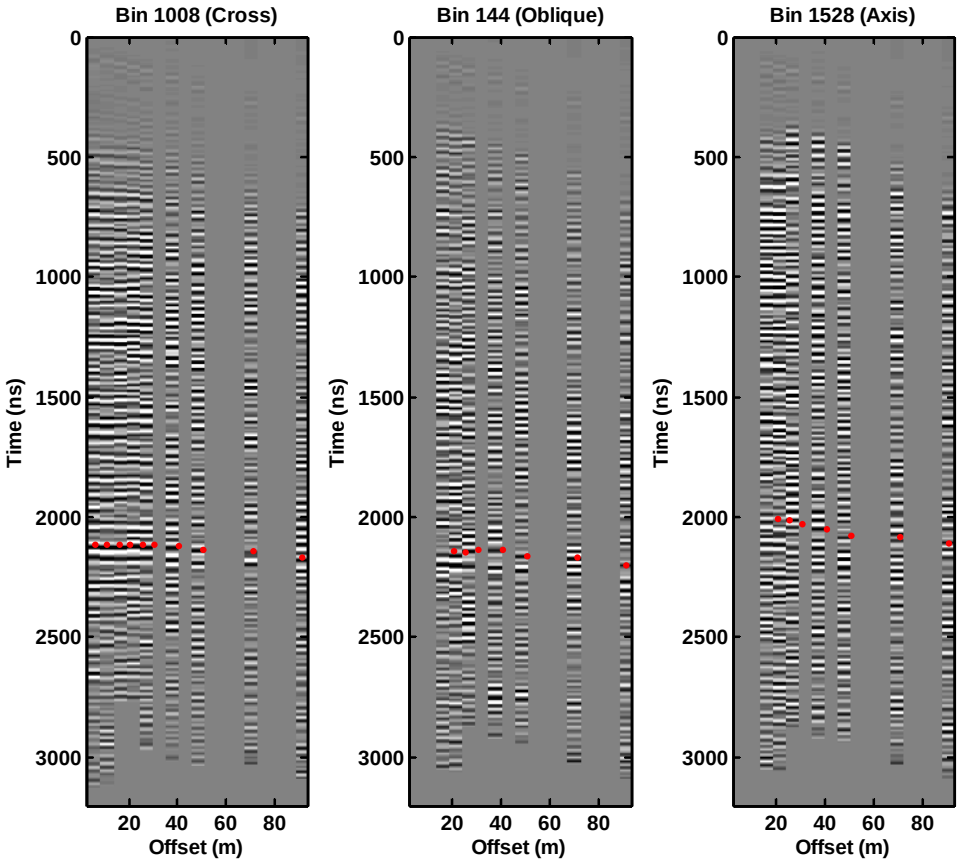

Figure 17 Processed CMPs showing bed reflection moveout for each azimuth.

Velocity Analysis

I read the data (bin number, offset and TWTT) into MATLAB, and grouped the offsets and TWTTs by azimuth and CDP. I squared the offset and TWTT, and fitted a line to that trend. The slope of the line is equal to one over the velocity squared. NMO corrected CMPs are shown in Figure 18. By determining the correct velocity the moveout of the bed reflection is flattened. Because of a lack of offsets and discrepancies in the geometry, many of the velocities were not realistic, including zero, velocities greater than the speed of light and imaginary velocities. Realistic glacial velocities are

between 0.14 m/ns and 0.18 m/ns (Bradford and Harper, 2005). Statistics for the realistic velocities are shown in Table 2.

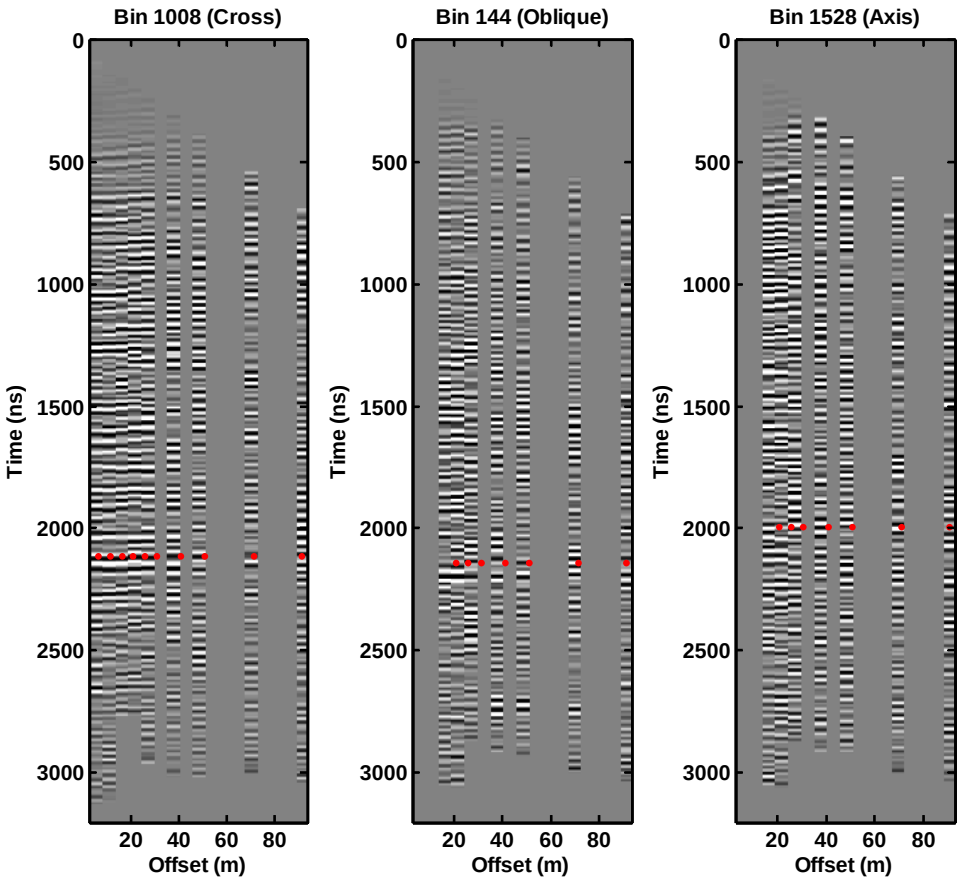

Figure 18 **NMO corrected CMP gathers. Note the flattened bed reflection by using the correct stacking velocity for each direction.**

Table 2 **Statistics for realistic velocities**

Azimuth	# of Velocity Estimates	Minimum (m/ns)	Maximum (m/ns)	Mean (m/ns)	Median (m/ns)	Standard Deviation	95% Range
Cross Glacier	748	0.140	0.180	0.1643	0.1655	0.0105	0.143-0.179
Oblique	590	0.140	0.179	0.1593	0.1584	.00118	0.140-0.1791
Glacier Axis	657	0.1402	0.180	0.1616	0.1626	0.0112	0.142-0.179

The distribution of the velocities is shown in Figure 19. The bin size for both the histogram and the kernel density function is 0.001 m/ns. While the range of velocities is similar for all three azimuths the distributions are significantly different. I used a Kolmogorov-Smirnov test to compare the distribution of velocities for each azimuth and found them to be from different distributions with greater than 95% confidence (Martinez and Martinez, 2008).

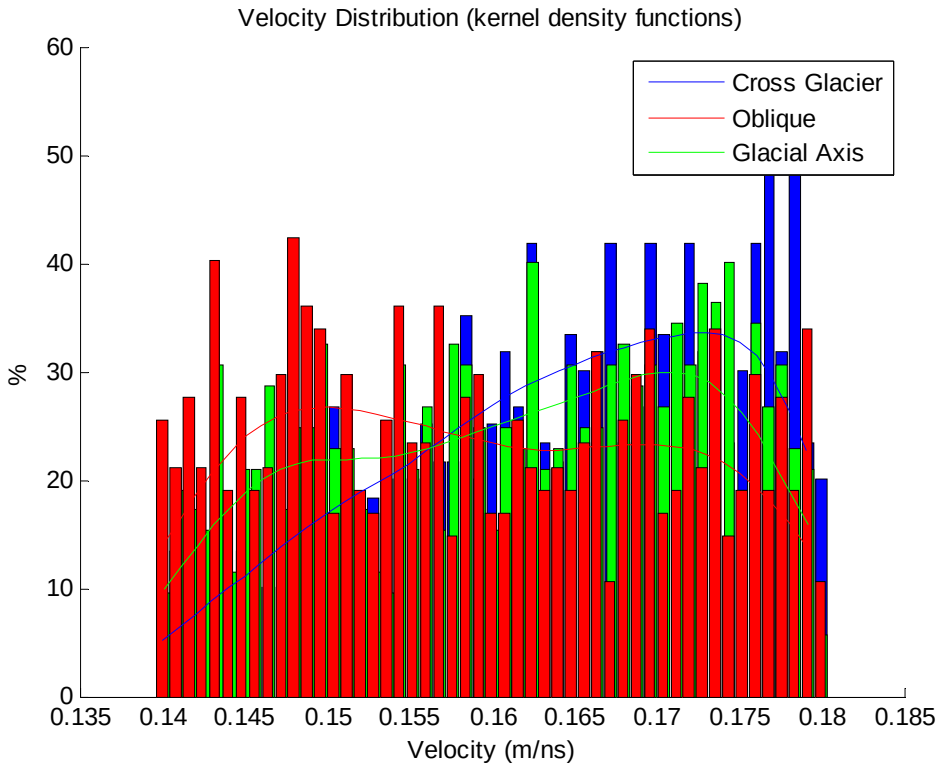

Figure 19 Distribution of velocity estimates

Uncertainty

To evaluate the uncertainty of the velocity estimates I performed a Monte-Carlo Bootstrap simulation (Martinez and Martinez, 2008). For this I used only bins containing more than 5 traces. I randomly sampled 5 traces from each bin 700 times, each time

calculating a velocity from those samples. If the velocity calculated using the 5 traces was between 0.14 m/ns and 0.18 m/ns, the value was recorded and saved. Table 3 shows some basic statistics on the velocities calculated using this method.

Table 3 Statistics from Monte-Carlo simulation

Azimuth	# Bins	Minimum	Maximum	Mean	Median	Standard Deviation	95% Range
Cross Glacier	1345	0.1403	0.1800	0.1646	0.1657	0.0093	0.145-0.178
Oblique	1021	0.1401	0.1796	0.1600	0.1592	0.0101	0.142-0.178
Glacier Axis	1377	0.1400	0.1799	0.1611	0.1620	.0101	.0142-0.178

Table 4 Standard Deviation for the average cell

Azimuth	Average # Velocity Estimates per bin	Minimum	Maximum	Mean	Median	Standard Deviation	95% Range
Cross Glacier	294	0	0.0182	0.0062	0.0062	0.0038	0-0.0132
Oblique	272	0	0.0167	0.0064	0.0068	0.0039	0-0.0131
Glacier Axis	263	0	0.0190	0.0064	0.0066	0.0037	0-0.0133

Table 4 shows statistics on the standard deviation of the calculated velocities for all bins with realistic velocities. The average standard deviation of the velocity per bin is approximately the difference between the median velocities in each direction. So while the standard deviation in velocities over the entire survey is greater than the degree of anisotropy, the average uncertainty in the calculated velocity in each bin is not. Figure 20 shows the distribution of velocity estimates from the Monte-Carlo simulation. Again

a Kolmogorov-Smirnov test proves the velocity distributions for each azimuth are from different distributions with greater than 95% confidence.

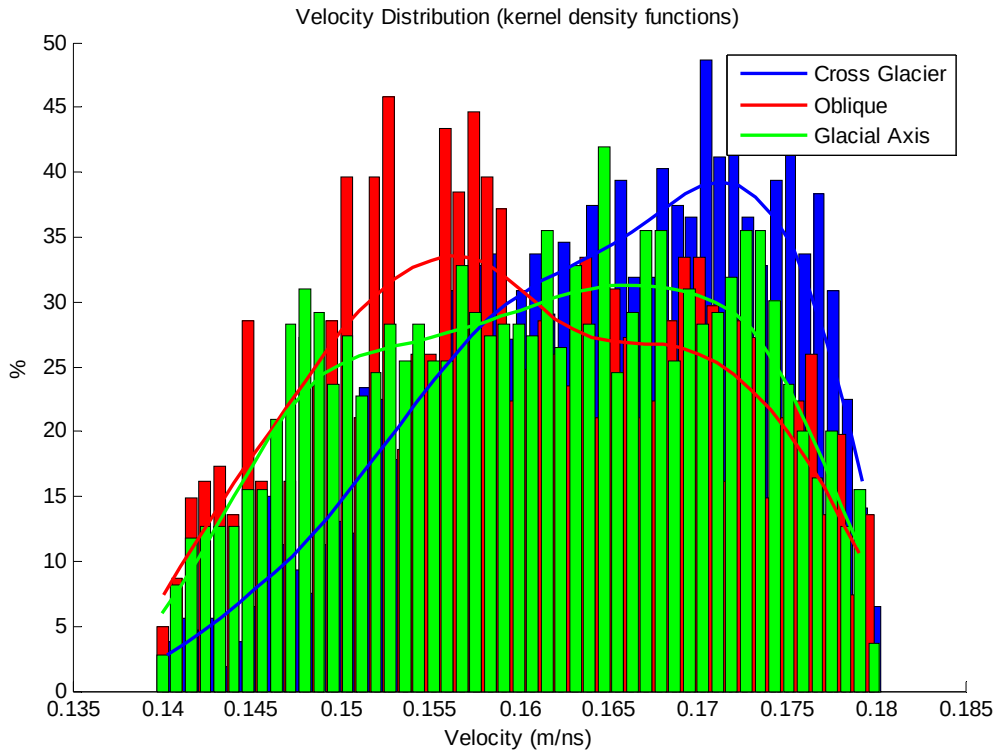

Figure 20 Distribution of velocity estimates from Monte-Carlo simulation

Spatial Variability

I also considered the spatial variability of the velocity estimates. To do this I plotted the experimental semivariogram for the velocities obtained from the Monte-Carlo simulation for each azimuth. I then tried different modeled variograms including spherical, linear and exponential models. Since there is no trend to the glacier axis, and oblique velocities, no model fit better than any other. The best fit for the cross glacier variogram was a spherical model (Figure 21).

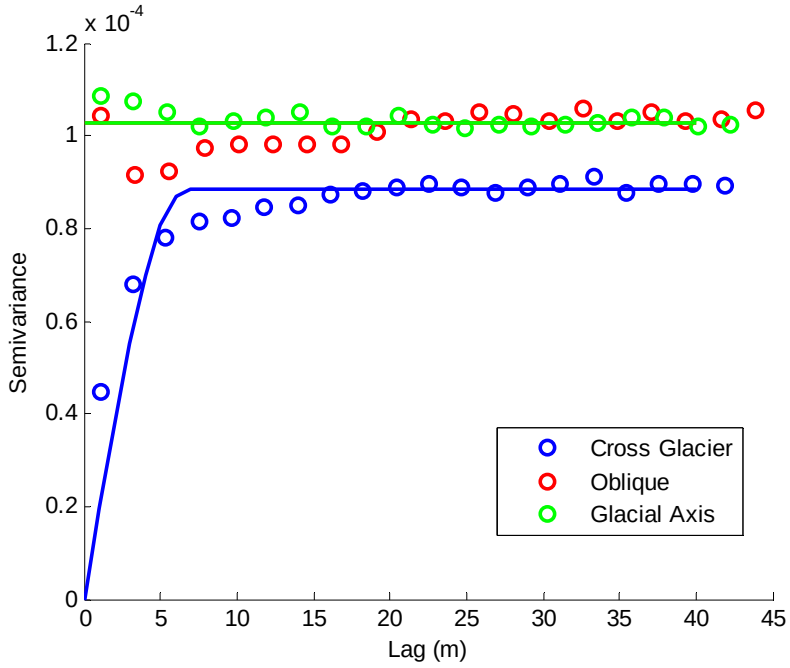

Figure 21 Semivariogram for velocities measured in each direction.

The lack of spatial coherence in velocity for oblique and along glacier axis, and the short range (~10 m) in the cross glacier direction indicates that interpretation of geostatistical analysis on this data will be challenging since we are using data from offsets that are greater than the scale of spatial coherence (i.e. the velocity likely changes within the CMP "footprint"). Using the variogram models, I used ordinary Kriging to estimate velocities in the bins where there was not a realistic velocity estimate. I also calculated the uncertainty in the estimates from Kriging. Note that for the Oblique and Glacier Axis directions, there is no spatial dependence, so uncertainties are high wherever the velocities are estimated by Kriging.

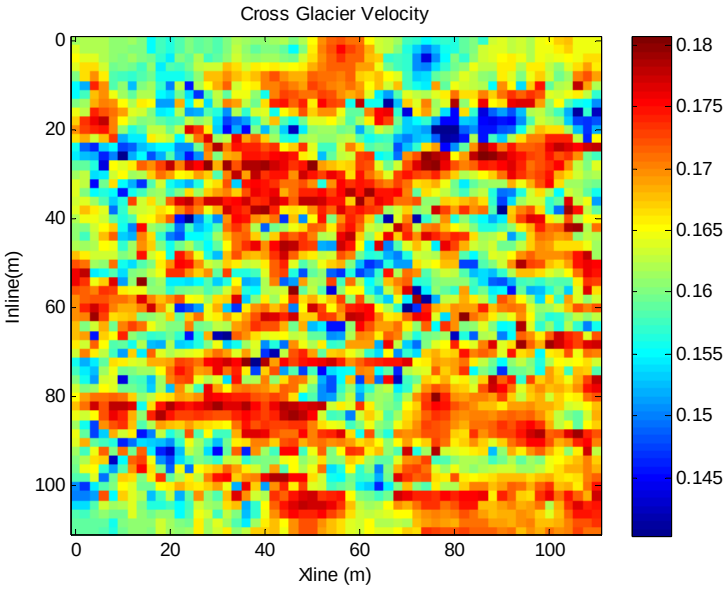

Figure 22 Velocity estimates for cross glacier direction, from ordinary Kriging.

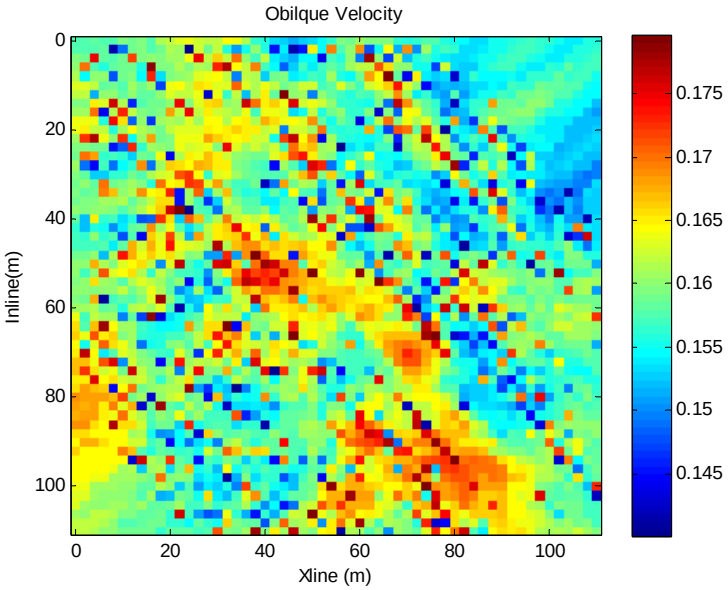

Figure 23 Velocity estimates for oblique direction, from ordinary Kriging.

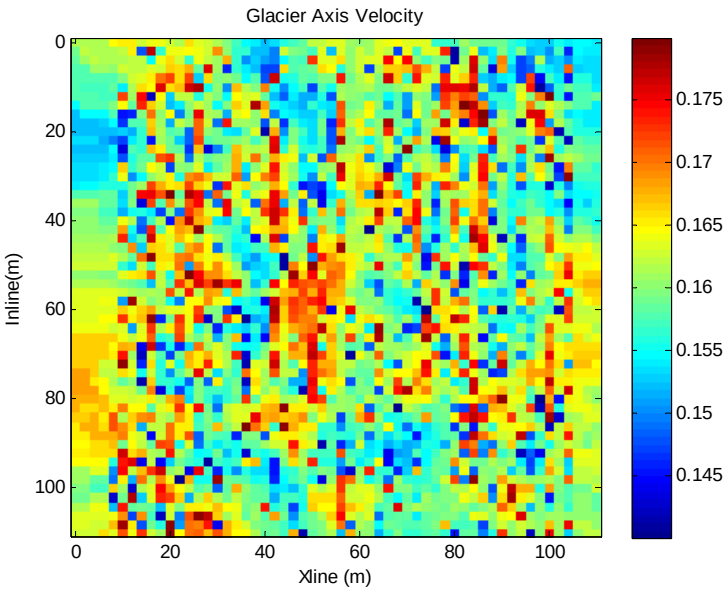

Figure 24 Velocity estimates for axial direction, from ordinary Kriging.

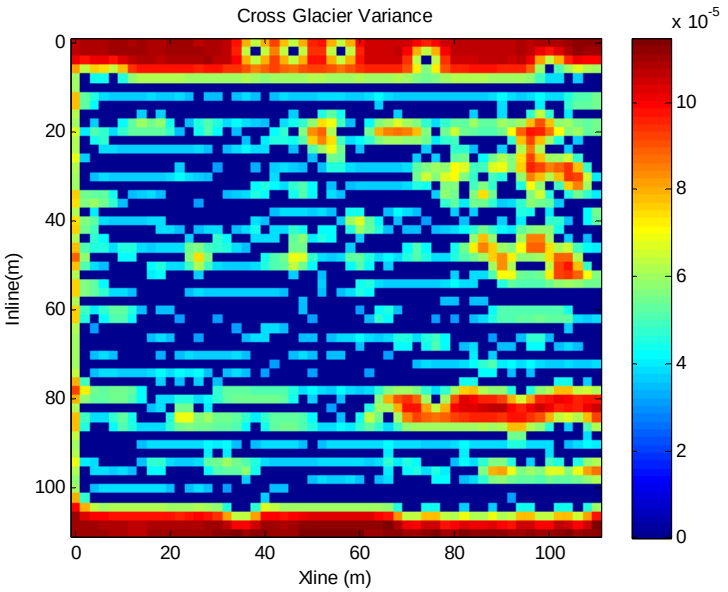

Figure 25 Variance in estimation from Kriging (cross glacier)

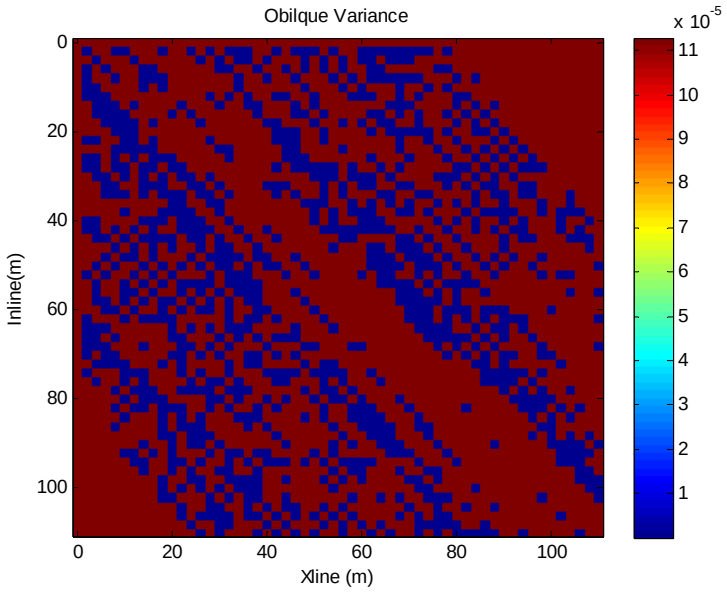

Figure 26 Variance in estimation from Kriging (oblique)

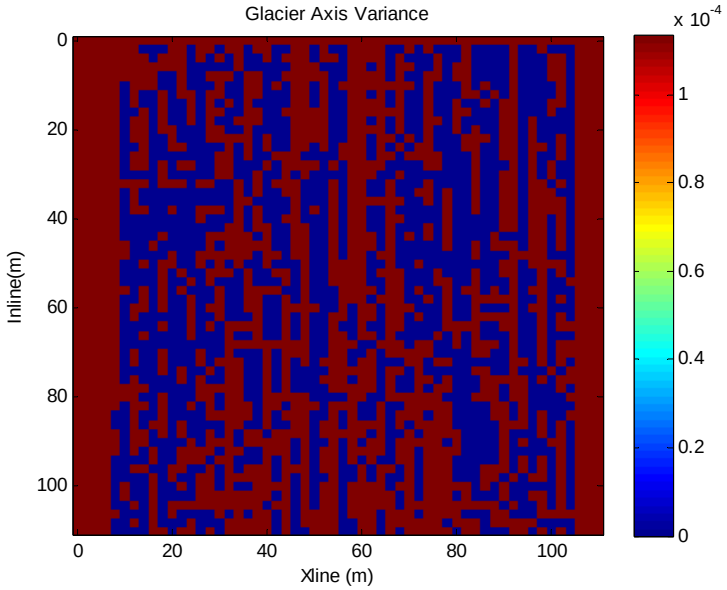

Figure 27 Variance in estimation from Kriging (glacier axis)

From the Kriging results there does not seem to be any strong spatial patterns. The most likely cause of this is the uncertainty in the geometry. Due to difficulty synchronizing the GPS clocks and the trace times, some of the traces could be placed in the incorrect bins, especially for the large offsets. I calculated velocities for large bins (ex. 4 m, 10 m, and 100 m); however uncertainties in the geometry produced unrealistic and inconclusive results.

Stacking and Migration

To get a better idea of the englacial structure, I produced a 3D stacked image of the survey site. The traces for all offsets and all three azimuths were sorted by bin. The data was stacked using an RMS velocity of 0.164 m/ns. This produced a continuous image of the bed beneath the survey area (Figure 28).

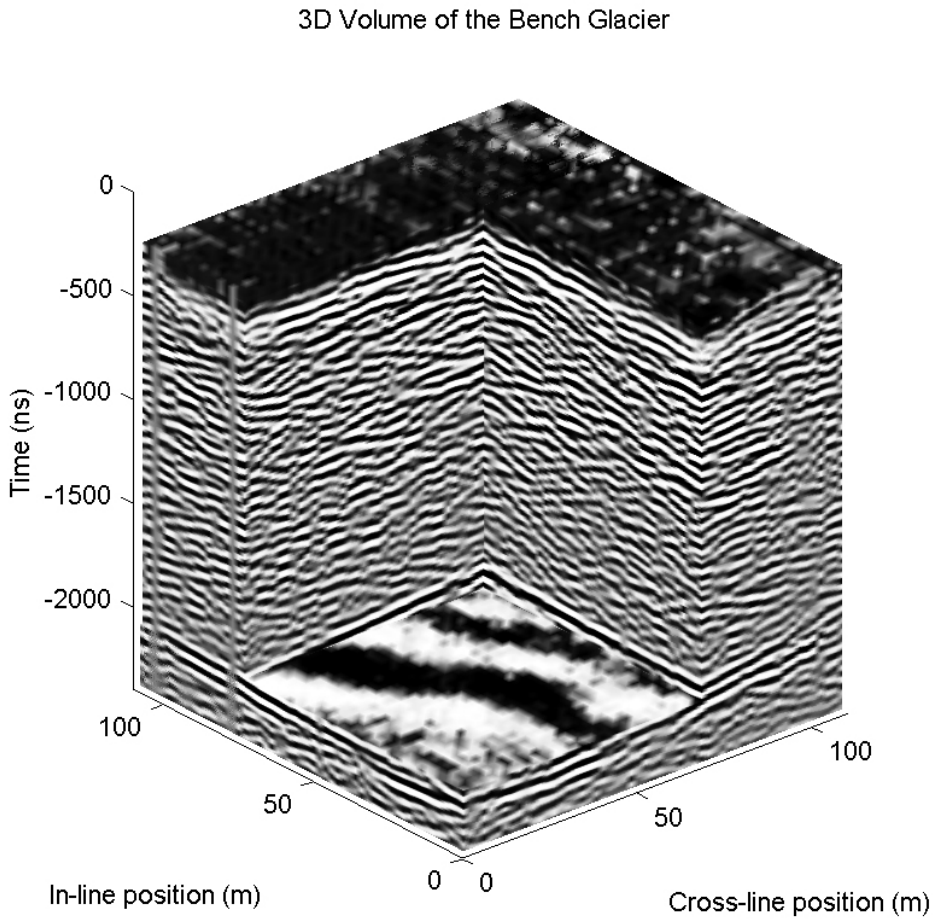

Figure 28 3D volume of 2006 survey site

I also stacked the data collected in each direction with the corresponding velocity. To get a true image of the bed and any internal structure, I migrated the data with a constant velocity phase-shift migration using the corresponding velocity from Table 3 (Gazdag, 1978). The orientation of the fractures can be seen in time slices of the migrated volume. Figure 29 is a time slice at 1088 ns of the migrated volume acquired across the glacier. Coherent linear events are interpreted to be water filled voids within the ice volume. These features can also be observed in the volume collected parallel to the glacier axis (Figure 30).

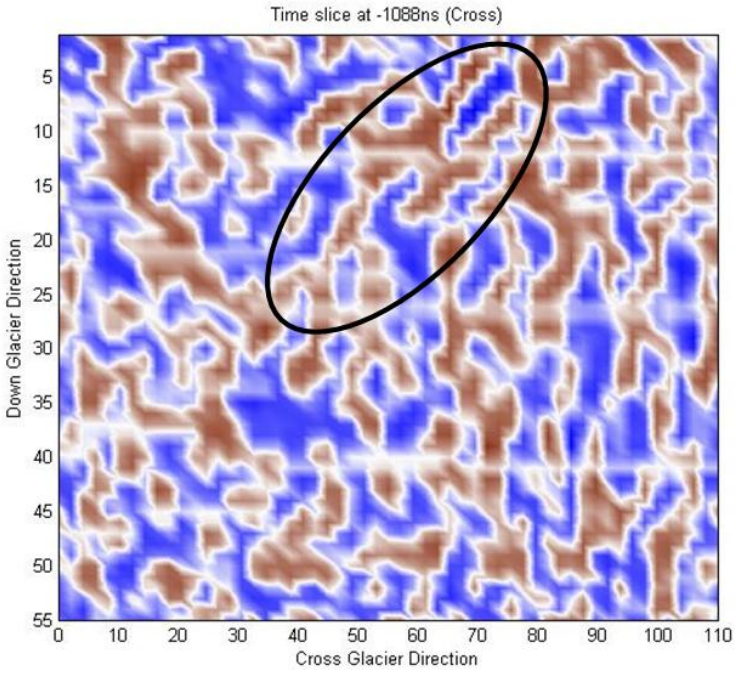

Figure 29 Time slice from migrated cross glacier volume showing fracture.

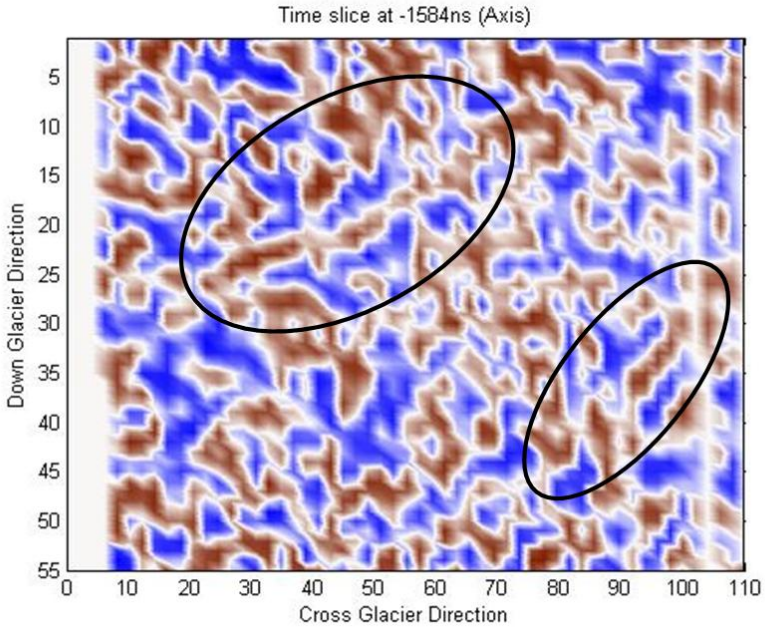

Figure 30 Time slice from migrated volume acquired parallel to the flow of Bench glacier. Imaged fractures are circled.

Wagon Wheel Survey Design and Data Collection

To further investigate these initial results, I designed a second survey to better quantify the anisotropy. In August 2008, I conducted the multi-azimuth, multi-polarization common midpoint survey approximately 200 m down glacier from the 3D grid. The location was varied to determine whether the anisotropy observed in the 3D survey was localized or more widespread. I collected common midpoint gathers in five different directions. In each direction I collected data from antennas with three different orientations. By changing the orientation of the antennas the polarization of the wave changes relative to the glacier. From Figure 12 it is clear that radar velocity is dependent on the polarization of the wave relative to aligned fractures. While this survey only looks at one midpoint, the angle and amplitude of anisotropy can be more easily determined than in the previous study. I designed this survey to provide data that could yield better insight into the relationship between fracture orientation and wave polarization. I collected data along five different azimuths: 0°, 14°, 38°, 64°, and 94° relative to cross-glacier (Figure 31). I collected three polarizations; yy-configuration (transverse electric), xx-configuration (transverse magnetic), and xy-configuration (cross-polarized) along each azimuth (Figure 32e, Figure 32a, Figure 32c respectively). I collected 3 radar traces every 2 m from 4 m to 200 m along each azimuth, with each antenna configuration. This survey used the Sensors & Software PulseEkko Pro system with 25 MHz antennas. Since this survey site had less coherent bed reflections than the 3D survey location, zero-offset profiles were collected in 2009 near the wagon wheel survey site (Figure 33). The 2D profiles were collected in multiple directions as well as multiple polarizations (Figure 34). Note that the bed reflection is much more obvious in profiles that are polarized in

the cross glacier direction, yy-configuration cross glacier and xx-configuration along the axis. This phenomenon is further evidence of anisotropic wave behavior of waves in a medium containing aligned inclusions. Multi-offset 2D profiles collected in 2006 with a yy-configuration along the axis of the glacier show a similarly masked bed reflection in this region (Figure 35). The zero-offset two-way traveltime can be determined from the 2d profiles so the correct reflection can be picked in the CMP gathers.

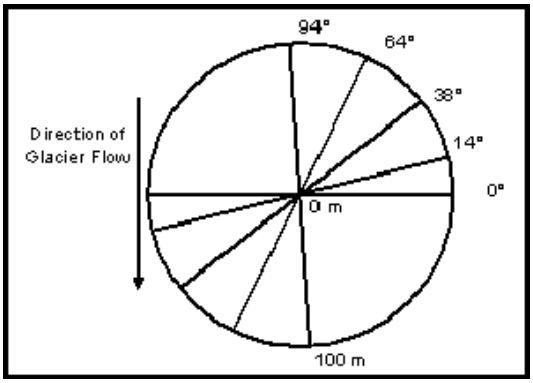

Figure 31 CMP Survey map, showing survey geometry and relationship to Bench Glacier

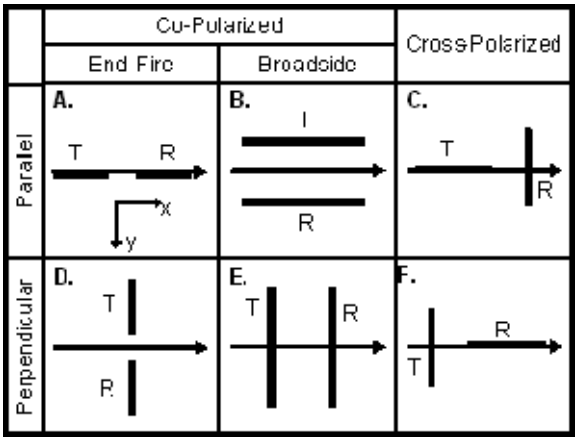

Figure 32 Representation of radar configurations. Adapted from Van Gestel and Stoffa (2001).

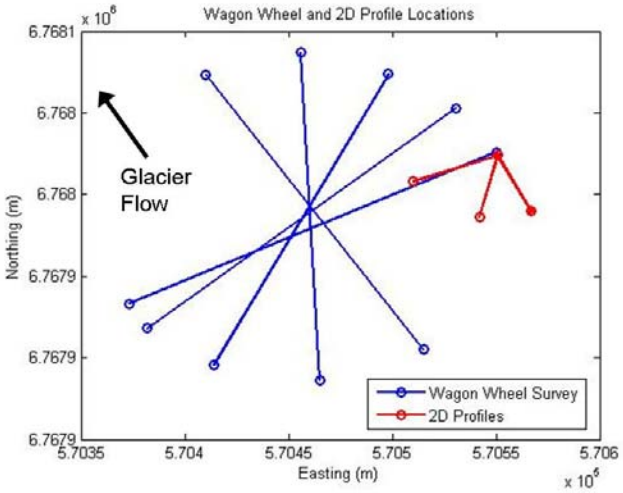

Figure 33 Map of wagon wheel and 2D survey lines

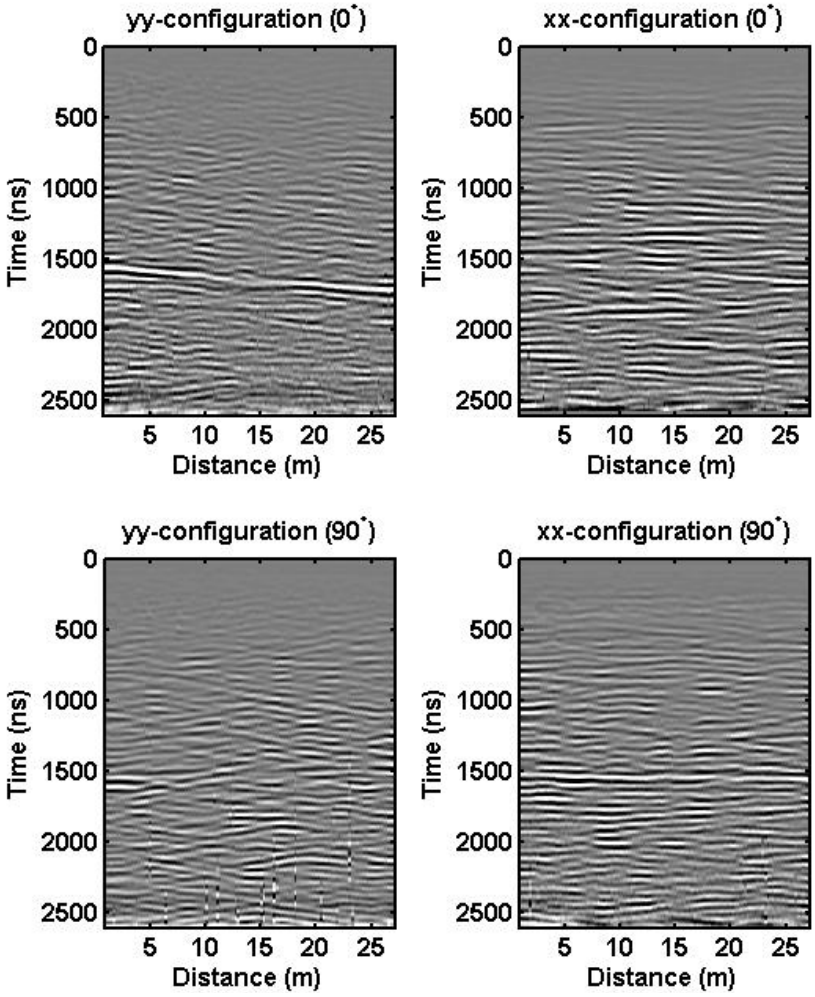

Figure 34 2D zero-offset profiles collected in the cross glacier and glacier axis directions near the CMP survey.

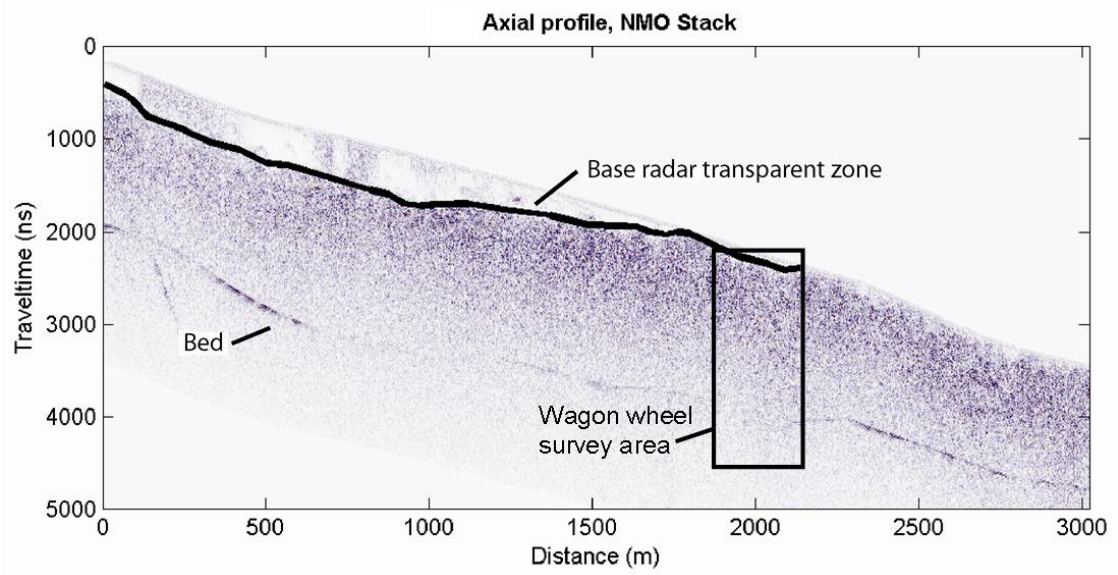

Figure 35 2006 multi-offset profile collected with yy-configuration along the glacier axis. Note the bed reflection in the area of the wagon wheel survey.

Wagon Wheel Data Processing

To evaluate the velocity in each direction I stacked the three shots at each location to increase the signal to noise ratio. I applied a 3-5-10-20 MHz bandpass filter as well as a true amplitude recovery ($g(t)=t^2$) to the data to emphasize the bed reflection and account for spreading. Figure 36 shows processed the processed CMPs collected along the 0º azimuth. The 2D profiles are processed the same way and provided the zero-offset TWTT to ensure the reflection resulting from the glacier bed was selected.

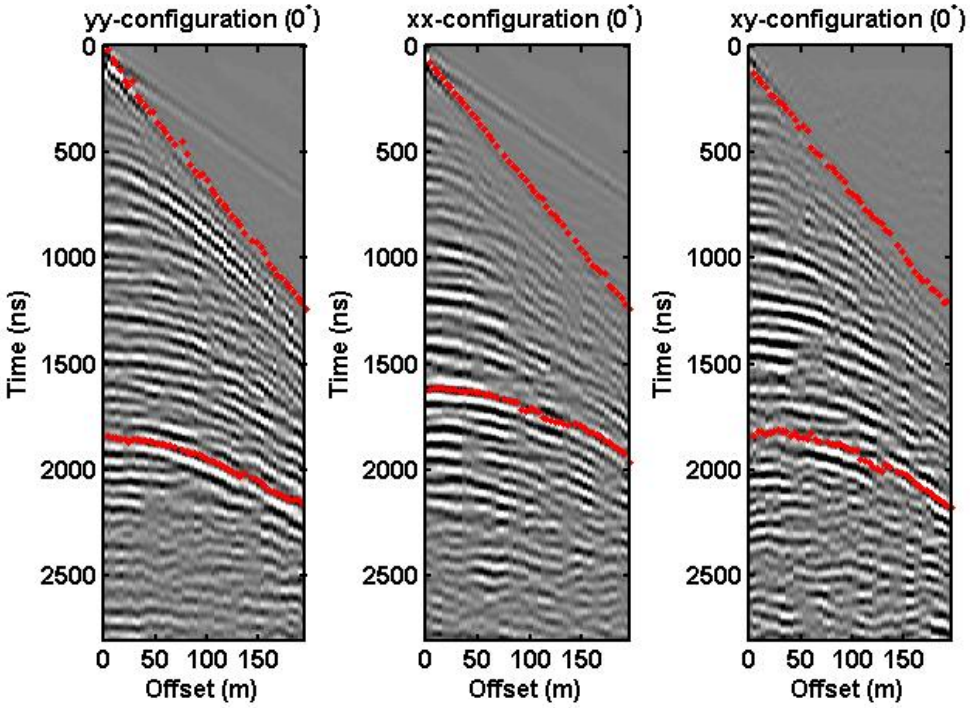

Figure 36 Processed CMP gathers for yy-, xx-, and xy-configurations, collected along the 0º azimuth. Direct-wave picks and TWTT picks of the bed reflection are shown in red.

Velocity Analysis

I then estimated the RMS velocity by fitting a hyperbola to the bed reflection using the NMO equation (Yilmaz, 2001). This was done for each polarization in each direction. In Figure 36 the same volume of the glacier is sampled, however the wave is polarized different due to the antenna configuration. Not only does the bed reflection moveout show the difference in velocity but so does the zero-offset TWTT. The direct wave does not exhibit any anisotropy associated with polarization of the wave (Figure 37). The variation in the velocity of the direct wave is due to air filled crevasses, moulins and water at the surface. Figure 38 shows the CMP gathers collected with antennas in the yy-configuration for the remaining azimuths. Figure 39 shows the bed reflection picks from data collected perpendicular to glacier flow using the yy-configuration. The error

bars represent the error in picking the peak of the wavelet (3 dB less than the maximum amplitude). An RMS velocity of 0.1727 m/ns was used to fit the data.

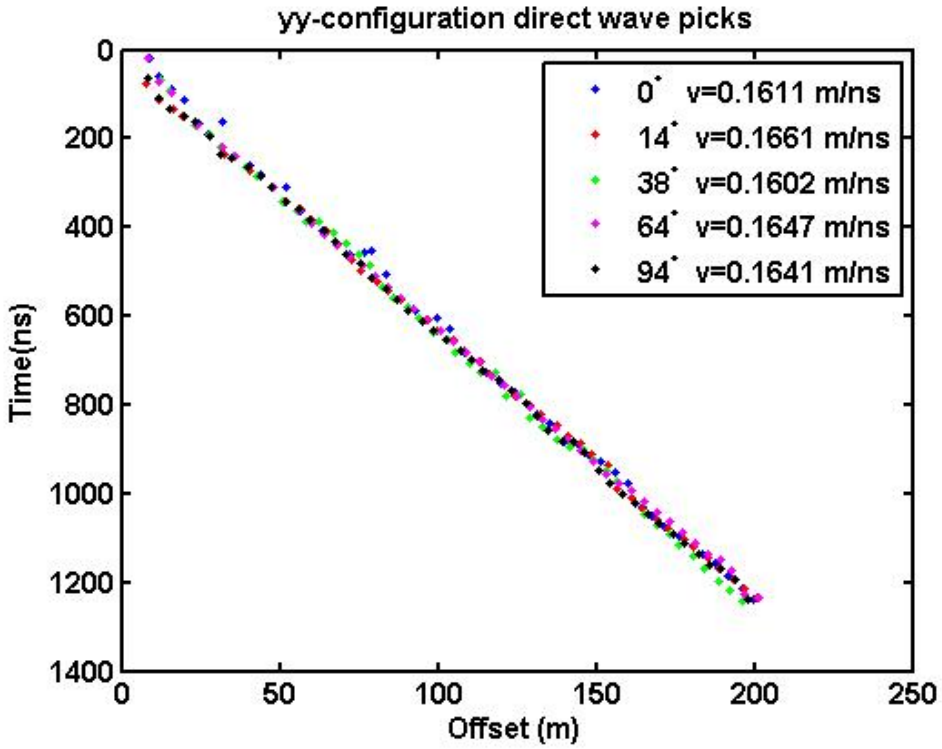

Figure 37 Direct wave travel times. The velocity fit to the direct wave does not exhibit anisotropy consistent with the anisotropy measured from the bed reflection.

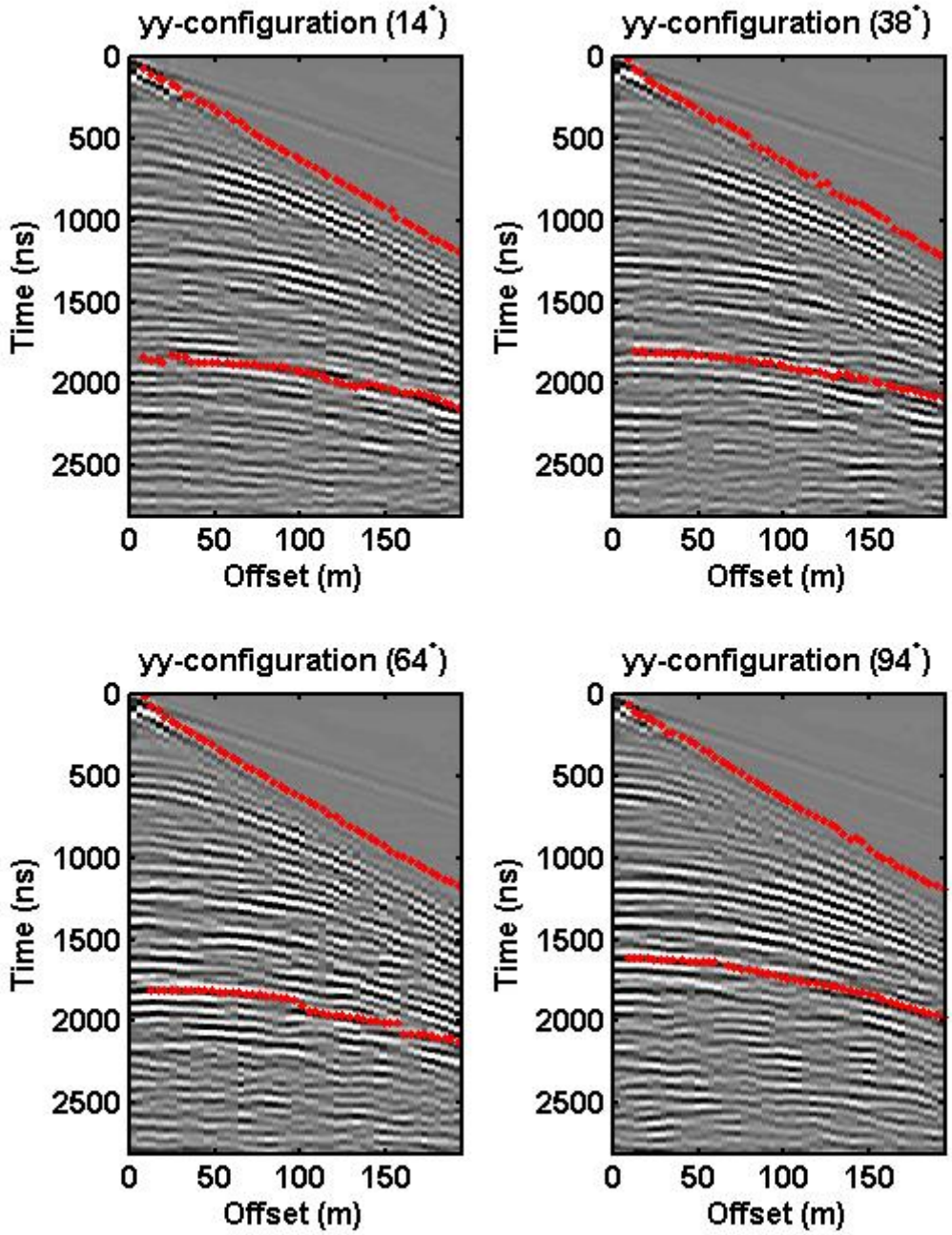

Figure 38 CMP gathers in the yy-configuration for the remaining azimuths with picks of the bed reflection and direct wave.

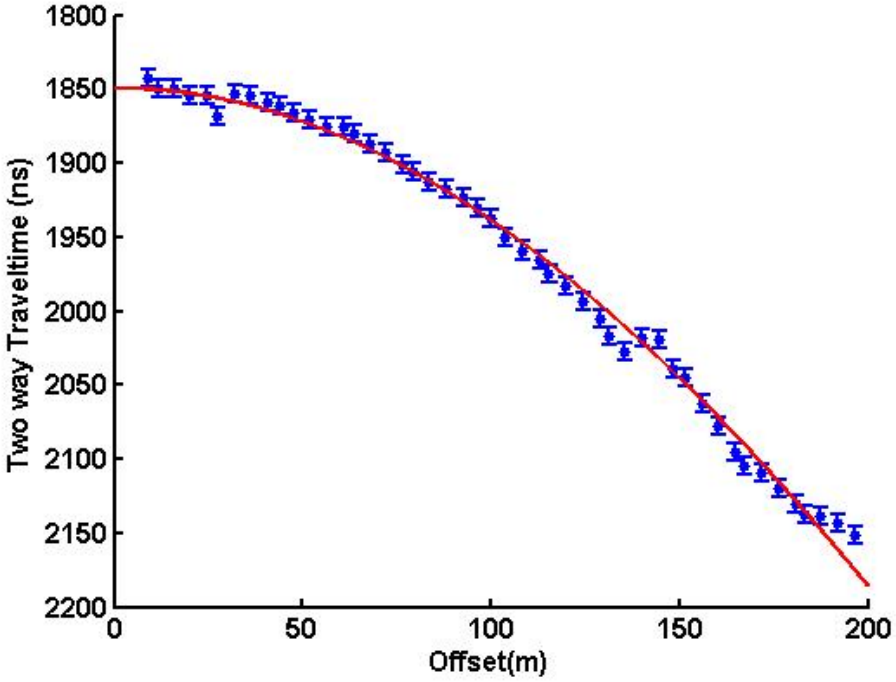

Figure 39 Bed reflection collected cross-glacier with the antennas in the yy-configuration. Picks of the bed reflection are shown in blue ± uncertainty in the peak amplitude. The hyperbola fit using 0.1727±0.002 m/ns shows good correlation with the bed reflection.

In addition to the voids, horizontal anisotropy could be present due to layering in the ice fabric. I investigated the potential for horizontal anisotropy, by observing the trend in velocities when including incrementally longer offsets in the fit. Figure 40 is a plot of the calculated velocities versus the maximum offset used in the fit. As expected, the error in estimating the velocity is greater at near offsets but, there is not a preference for over- or under-estimating the velocity regardless of the direction of polarization or propagation.

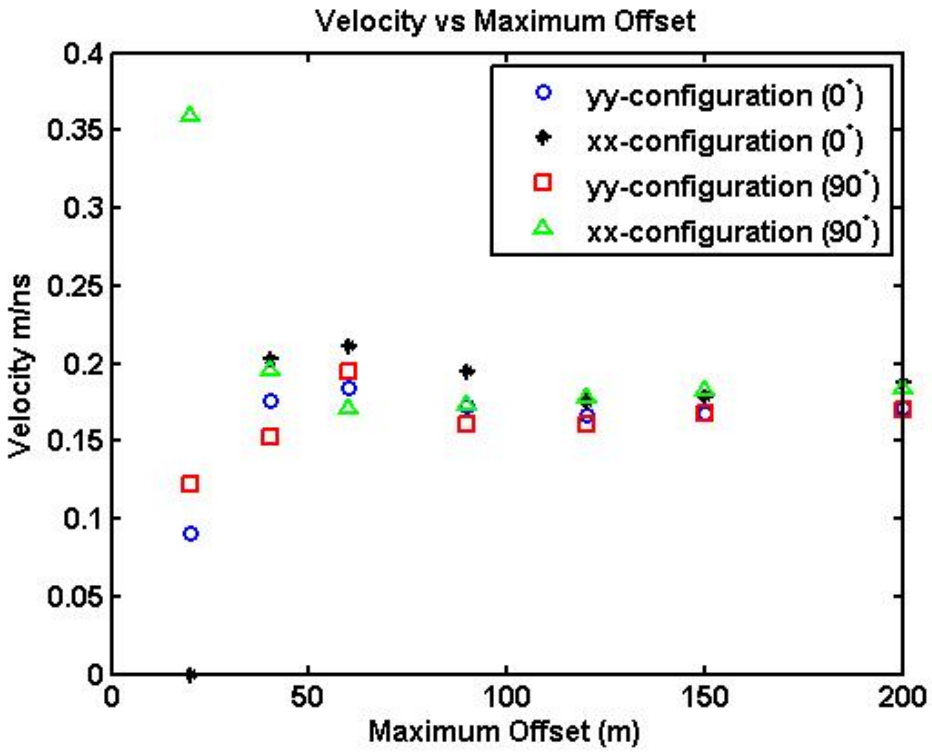

Figure 40 Velocities calculated with varying ranges of offsets for 0º and 90º for the yy- and xx-configurations. The variation in velocity does not appear dependent on the maximum offset used in the fit.

Wagon Wheel Uncertainty

To better asses the uncertainty associated with the fit of the velocity, and the sensitivity to individual TWTT measurements, I performed a Delete-d Jackknife Monte Carlo simulation. For this simulation I removed the first 15 offsets from each CMP gather and calculated the velocity fitting the remaining TWTT. I then removed offsets 2-16, 3-17, 4-18 and so on, each time determining the best fit velocity. I then calculated the average of these velocities as well as the standard error for each CMP and polarization (Table 5). The apparent anisotropy is greater than the uncertainty for each direction and polarization.

Table 5 Uncertainties in the velocity estimate.

Angle	yy-configuration velocity (m/ns)	xx-configuration velocity (m/ns)	xy-configuration velocity (m/ns)	yy-configuration standard error (m/ns)	xx-configuration standard error (m/ns)	xy-configuration standard error (m/ns)
0	0.1727	0.1869	0.1667	0.0009	0.0025	0.0032
14	0.1793	0.1686	0.1704	0.0021	0.0015	0.0023
38	0.1866	0.1677	0.1880	0.0036	0.0029	0.0040
64	0.1680	0.1651	0.1811	0.0048	0.0022	0.0018
94	0.1701	0.1846	0.1689	0.0022	0.0017	0.0041

Chapter Review

I designed two georadar surveys to investigate velocity anisotropy on Bench Glacier. The 2006 survey covers a 100m by 100 m grid. Processing and velocity of this survey show that the maximum velocity is 0.168 m/ns and oriented 33º relative to cross glacier. The 2008 multi-azimuth multi-polarization CMP survey estimates the velocity at only one location, but with high precision. The maximum velocity in the yy-configuration is 0.186 m/ns and oriented at 33.5º relative to cross glacier. Both surveys show azimuthally dependant velocities and are consistent with each other as well as previous observations.

CHAPTER FOUR: INTERPRETATION AND DISCUSSION

3D Interpretation

The 2006 survey produced a 3D image of Bench Glacier. After minimal processing, the bed reflection was continuous throughout the survey in each of the three azimuths. The velocity in each direction can be determined by gathering the traces into bins and sorting them by azimuth. The velocities throughout the survey site show azimuthal dependence. The most likely scenario that would cause such wide spread anisotropy is oriented water-filled fractures distributed throughout the glacier. The uncertainty for each individual bin is less than the degree of anisotropy; however the uncertainty in velocity estimates over the entire grid is greater. The survey site was selected to minimized dip, and other heterogeneities at the bed. The dip of the bed under this survey site is ~6º, determined from the migrated section in Bradford et al. (2009). Using equation 13 (Yilmaz, 2001) the NMO velocity from the apparent velocity and the angle of the dip can be determined:

$$v_{NMO} = \frac{v}{\cos(\phi)} \qquad (13)$$

V_{NMO} is the corrected NMO velocity based on the apparent velocity (v), and the dip of the reflector (ϕ). For a dip of 6º the NMO velocity is <1% less than the apparent velocity. For a 10º slope (average for Bench Glacier), the NMO velocity is <2% less than the apparent velocity. This difference in apparent vs. NMO velocity does not account for the anisotropy measured in Bench Glacier in magnitude or direction. Another way to

reduce the uncertainty would be better constraint of the survey geometry. Due to the synchronization of the GPS time and trace times, accuracy in the geometry was compromised. The uncertainty resulting from incorrect offsets can be estimated by plotting the partial derivative with respect to offset versus the assumed offsets used in determining the velocity (Figure 41). From this curve the uncertainty in the velocities calculated with offsets up to 70 m that have an error of 1 m is ~0.004 m/ns, which is less than the amount of anisotropy observed in the 3D data. If the offset measurement were off by 10 m this would translate to an uncertainty ~0.04 m/ns, sufficiently masking anisotropy on the scale observed in Bench glacier.

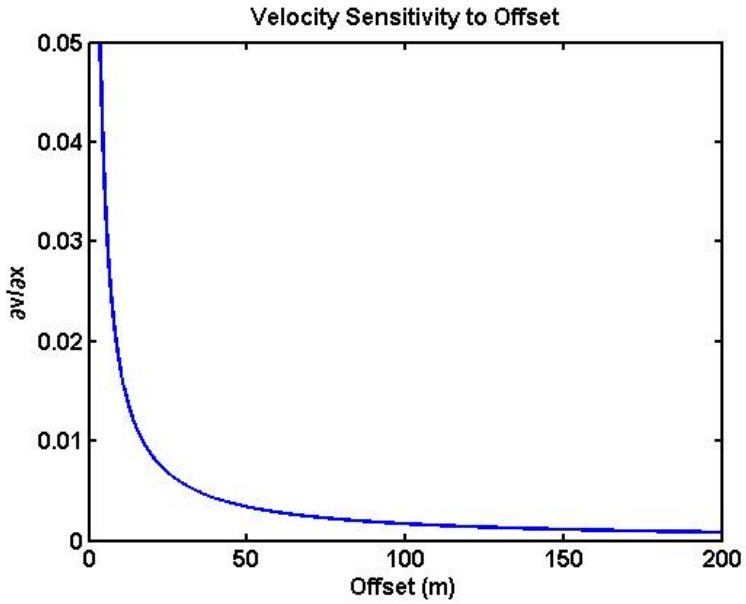

Figure 41 The partial derivative of velocity as a function of offset.

Based on the velocities estimated by the Monte-Carlo simulation we can plot an ellipse to determine the direction and amplitude of the maximum velocity (Figure 42). The ellipse is generated by a direct least squares fit algorithm developed by Fitzgibbon et al. (1999). The direction of the maximum amplitude agrees well with the void orientation

measured in boreholes. The maximum velocity is 0.168 m/ns oriented at 33.65º relative to cross glacier. The minimum velocity is 0.158 m/ns and is perpendicular to the direction of maximum velocity. If a georadar survey conducted with the waves propagating roughly 33º relative to cross glacier, and the medium was assumed to have isotropic dielectric permittivity, the water content would be 2.6%. If the same survey were conducted perpendicular to that survey, again assuming isotropy, the measured water content would be 1.0%. By acknowledging the anisotropic velocity of waves propagating through preferentially aligned water filled fractures (approximated as disks) a better estimate of the water content is 2.0%.

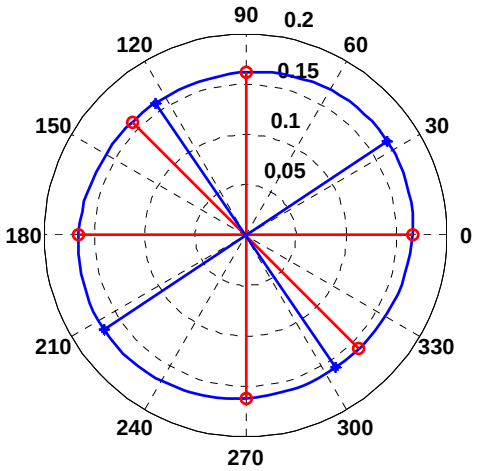

Figure 42 Velocity ellipse based on Monte-Carlo velocities.

Wagon Wheel Interpretation

The velocities for each direction and polarization are shown in Table 5. By measuring the RMS velocity above the bed reflection and fitting an ellipse to the velocity vs. azimuth data, I determined the magnitude and direction of the maximum velocity (Figure 43). The ellipse is generated by a direct least squares fit algorithm developed by

Fitzgibbon et al. (1999). The ellipses also show the magnitude of the minimum velocity, which is perpendicular to the maximum. The yy-configuration shows almost 20% anisotropy oriented at 33.5° to glacier flow. The xx-configuration has a similar degree of anisotropy oriented perpendicular to the maximum of the yy-configuration. Since the wave from the xx-configuration is polarized perpendicular to that of the yy- and xy-configuration, the direction of maximum velocity should also be perpendicular to that of the yy- and xy-configuration. The maximum velocities, minimum velocities and directions are reported in

Table 6.

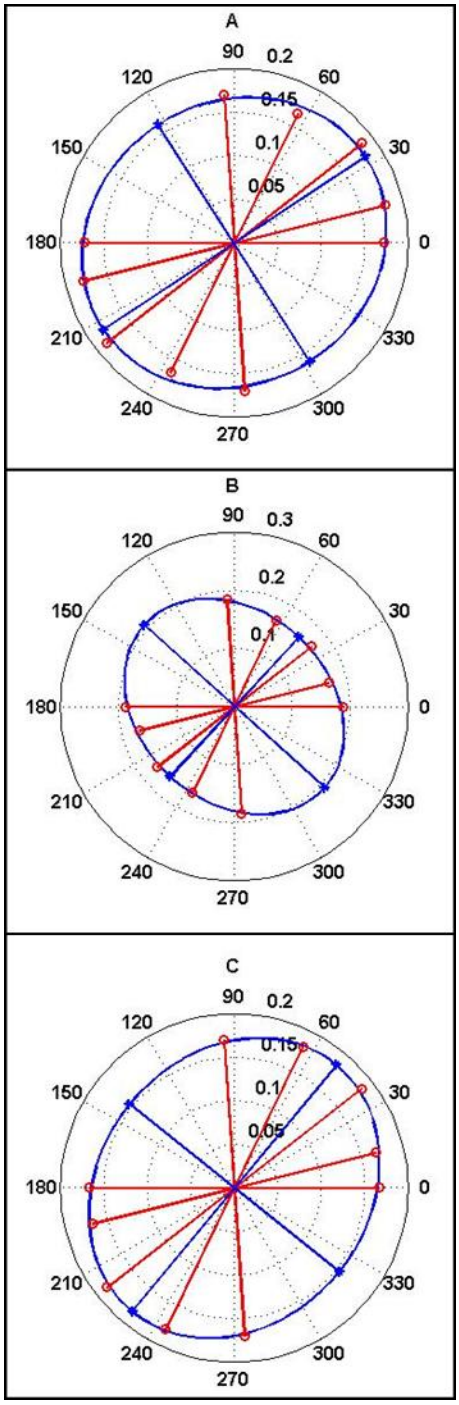

Figure 43 The ellipses show the azimuthal dependence of radar velocity. "A" shows velocities for the yy-configuration. "B" shows the velocities for the xx-configuration and "C" for the xy-configuration. The maximum velocity in "A" is directed perpendicular to the maximum in "B".

Table 6 The RMS velocities (m/ns) measured above the bed reflection for each polarization and azimuth. v_{min} and v_{max} are based on the ellipse fit. The direction is measured relative to the cross glacier direction.

Angle	yy-configuration velocities (m/ns)	xx-configuration velocities (m/ns)	xy-configuration velocities (m/ns)
0	0.1716	0.1873	0.1794
14	0.1794	0.1689	0.1682
38	0.1864	0.1680	0.1856
64	0.1661	0.1653	0.1805
94	0.1700	0.1843	0.1687
v_{max} from fit	0.1807	0.2097	0.1843
v_{min} from fit	0.1618	0.1639	0.1546
Direction of v_{max}	33.5º	137.9º	50.3º

Radar Discussion

Radar waves are known to exhibit anisotropic reflection amplitudes and phase shifts (Van Gestel & Stoffa, 2001; Nobes, 1999; Sassen & Everett, 2009; Tsoflias et al., 2004). There is also theory showing anisotropy in the bulk dielectric permittivity resulting from preferentially aligned inclusions (Taylor, 1965; Giordano, 2005). Here I have shown that this anisotropic permittivity is significant enough to result in measurable anisotropic wave velocities. Through two different surveys, I found that the maximum velocity is aligned parallel with the orientation of the inclusions that have a higher permittivity, which agrees with what could be inferred from Giordano (2005). The 2006 survey was limited by constraints on the source receiver geometry. However it did provide evidence that velocity anisotropy is widespread, and fairly constant in a mixture with oriented inclusions. The 2008 wagon wheel survey, which has higher accuracy in the geometry and offsets, also shows anisotropic velocities. Additionally the 2008 survey samples the same part of the glacier with waves that are polarized perpendicular to each other. This eliminates any uncertainty associated with sampling different parts of the subsurface. Both the anisotropy observed by changing polarization as well as changing

azimuth agrees with the 2006 survey and Giordano (2005). In both surveys the direct wave did not exhibit significant anisotropy, so any anisotropy must come from the sampled medium, and not from surface effects. An example of the direct wave is shown from the CMP survey in Figure 36 and Figure 38. Figure 44 shows the anisotropy ellipse for the 2006 survey, the xx-configuration of the 2008 survey as well as the observed void orientation from boreholes.

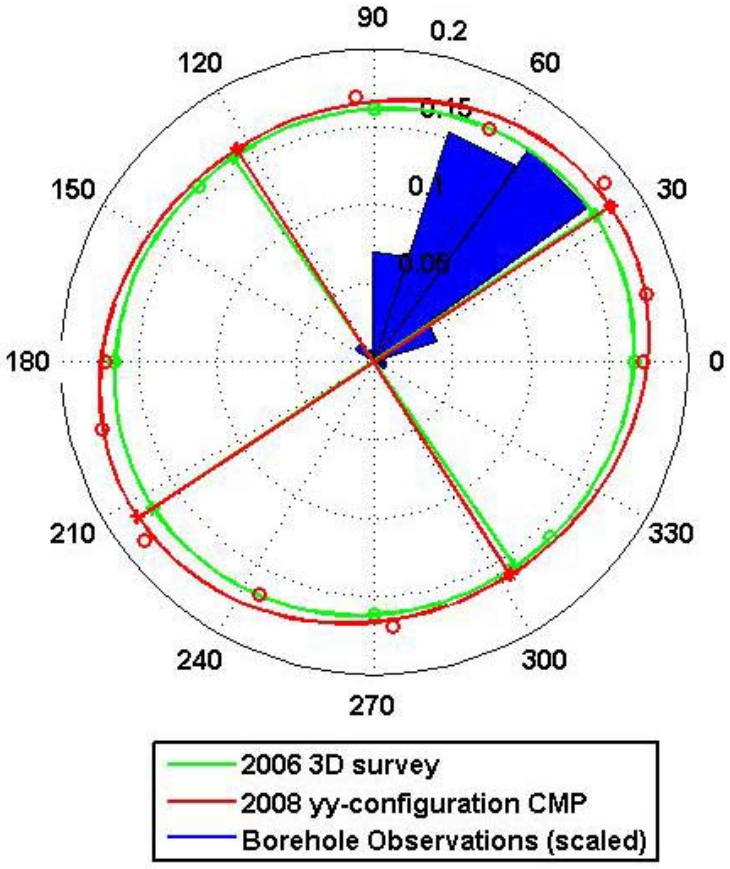

Figure 44 Borehole observations with velocity ellipses from 2006 and 2008 surveys.

Glaciological Discussion

Temperate glaciers have water filled voids distributed throughout the ablation zone. From borehole measurements and now azimuthally dependant radar studies we know these inclusions have preferential orientation. This has significant implications for surveys using radar velocity to determine depth to the bed and water content. Radar can still be used, but the preferred direction of the voids, must be known. If Bench glacier were assumed to be isotropic and was surveyed parallel to the fast direction, the glacier would have an average RMS velocity of 0.173 ± 0.006 m/ns. The estimated water content would be 0.3 ± 2% using the depth dependent mixing model (equations 2 and 3.). If surveyed parallel to the slow direction the average RMS velocity would be 0.151± 0.008 m/ns leading to a water content estimate of 3.8 ± 1.5%. Thus two surveys over the same area would yield two different water content estimates. If anisotropy is assumed, then at least one more direction must be surveyed to calculate a velocity ellipse, and the water content estimate would be more accurate. By determining the velocity of waves polarized in three different directions, and fitting an ellipse to those, the direction and magnitude of the slow and fast velocities can be determined. Additional information is needed to determine the degree of order; in this case I used previous studies, migrated images, and borehole observations. From the multi-azimuth velocities and an order estimate the water content can be better constrained. For the case of Bench glacier, I calculated the degree of order to be 0.9 (void orientation varies less than 15º from the mean), and using a slow velocity of 0.151 m/ns and a fast velocity of 0.173 m/ns, the water content is 1.2 ± 0.6%. From the literature, water content estimates range from 0-9% (Petterson et al., 2004). While most water content estimates on a single glacier varied

by less than 2% total volume, some estimates of the water content ranged from 0.5-7.6% for one glacier (Petterson et al., 2004). While the orientation and order of the voids is not known for those cases, by assuming a preferred orientation of the voids, one can argue that the uncertainty in the measurement is not as high as it would appear. Instead both water content estimates assuming isotropy can be thought of as a measurement in the slow and fast direction of an azimuthally dependent velocity model. In this case the slow velocity is ~0.148 m/ns and the fast direction ~0.168 m/ns assuming spherical voids, and a depth dependent air concentration. Using these two velocities, and assuming disks with a preferred orientation similar to Bench glacier, the estimated water content is no longer a range but instead ~3.5%.

Conclusions

As shown in Figure 44 both radar surveys exhibit velocity anisotropy consistent with the direction of the voids. This anisotropy is apparent even with a water concentration as low at 1%. Obviously the sensitivity of the anisotropy is dependant on the difference between the dielectric permittivities. This method does have its limitation, in that the degree of order and preferred orientation cannot be determined from a single survey using only radar velocities, in this case study, borehole video was used to constrain the degree of order of the voids. As with any analysis based on radar velocities the geometry plays an important role in minimizing the uncertainty.

REFERENCES

Annan, A.P., 2005,Ground-Penetrating Radar, in Near-Surface Geophysics, edited by D.K. Butler, Investigations in Geophysics, No. 13, Society of Exploration Geophysicists, Tulsa, OK, 357-438.

Arcone, S.A., Yankielun, N. E., 2000, 1.4 GHz radar penetration and evidence of drainage structures in temperate ice: Black Rapids Glacier, Alaska, USA: Journal of Glaciology, 46, 47-490.

Arendt A.A., K. A. Echelmeyer, W.D. Harrison, W.D. Lingle, and V.B. Valentine, 2002, Rapid wastage of Alaska glaciers and their contribution to rising sea level: Science, 297, 382-386.

Bailey, J.T., S. Evans and G. de Q Robin, 1964, Radio echo sounding in polar ice sheest: Nature, 204, 420-421.

Barrett, B.E., T. Murray, R. Clark, and K. Matsuoka, 2008, Distribution and character of water in a surge-type glacier revealed by multifrequency and multipolarization ground-penetrating radar, Journal of Geophysical Research, 113, F04011.

Barrett, B.E., T. Murray, and R. Clark, 2007, Errors in radar CMP velocity estimates due to survey geometry, and their implication for ice water content estimation: J. Environ. Eng. Geophys., 12(1) 101-111.

Benjumea B. and T. Teixido, 2001, Seismic reflection constraints on the glacial dynamics of Johnsons Glacier, Antarctica, Journal of Applied Geophysics, 46(1), 31-44.

Betterly, S. J., Speece, M. A., Levy, R. H., Harwood, D. M., and Henrys, S. A., 2007, A novel over-sea-ice seismic reflection survey in McMurdo Sound, Antarctica, Terra Antarctica, 14(2), 97-106.

Bradford, J. H., and J. T. Harper, 2005, Wavefield Migration as a Tool for Estimating Spatially Continuous Radar Velocity and Water Content in Glaciers: Geophysical Research Letters, *32*, L08502, doi:08510.01029/02004GL021770.

Bradford, J.H., Nichols, J., Mikesell, D., Harper, J., 2009, Continuous multi-fold acquisition and analysis of ground-penetrating radar data for improved characterization of glacier structure and water content: Annals of Glaciology, 50(51), 1-9.

Brown, J.M., J.T.Harper, J. Bradford, 2009, A radar transparent layer in a temperate valley glacier: Bench Glacier, AK: Earth Surface Processes and Landforms, 34, 1497-1506.

Endres, A.L., T. Murray, A.D. Booth, and L.J. West, 2009, A new framework for estimating englacial water content and pore geometry using combined radar and seismic wave velocities, Geophysical Research Letters, 36, L04501.

Fitzgibbon, A., Maurizio, P. and B. Fisher, 1999, Direct least-squares fitting of ellipses: IEEE Transactions on Pattern Analysis and Machine Intelligence, 21(5), 476-480.

Fountain, A.G. and J.S. Walder, 1998, Water flow through temperate glaciers: Rev. Geophys., 36(3), 299–328.

Fountain, A.G., Schlicting, R.B., Jacobel, R.W., and Jansson, P., 2005, Fractures as main pathways of water flow in temperate glaciers: Nature, 433, 618-621.

Fudge, T. J., N. F. Humphrey, J. T. Harper, and W. T. Pfeffer, 2008, Diurnal Fluctuations in Borehole Water Levels: Configuration of the Drainage System Beneath Bench Glacier, Alaska: Journal of Glaciology, *54*(185), 297-306, doi 210.3189/002214308784886072.

Gazdag, J., 1978, Wave-equation migration by phase shift: Geophysics, 42, 1342-1351.

Giordano, S., 2005, Order and disorder in heterogeneous material microstructure: Electric and elastic characterization of dispersions of pseudo-oriented spheroids: International Journal of Engineering Science, 43, 1033-1058.

Harper, J. T., J. H. Bradford, N. F. Humphrey, T. W. Meierbachtol, and W. T. Pfeffer, 2008, Fractures As An Extension Of The Subglacial Drainage System, in Workshop on the Mass Balance and Dynamics of Arctic Glaciers, *e*dited by J. Oerlemans and C. Tijm-Reijmer, pp. 57-59, Institute for Marine and Atmospheric Research, Utrecht University, The Netherlands, Obergurgl, Austria.

Harper, J. T., N. F. Humphrey, W. T. Pfeffer, and B. Lazar, 2007, Two modes of Accelerated Glacier Sliding Related to Water: Geophysical Research Letters, *34*(12), L12503, doi:12510.11029/12007GL030233.

Harper, J. T., N. F. Humphrey, W. T. Pfeffer, T. Fudge, and S. O'Neel, 2005, Evolution of subglacial water pressure along a glacier's length: Annals of Glaciology, 40, 31-36.

Jacobel, R., Raymond, 1984, C. Radio echo-sounding studies of englacial water movement in Variegated Glacier, Alaska: Journal of Glaciology, 30, 22-29.

Johannessen, Ola M.; Khvorostovsky, Kirill; Miles, Martin W.; Bobylev, Leonid P., 2005, Recent Ice Sheet Growth in the Interior of Greenland, Science. 10.1126/science.1115356

Jol, H.M., 2009, *Ground Penetrating Radar: Theory and Applications*, 544 pp., Elsevier, Oxford, UK.

Kovacs, A., and R.M. Morey, 1978, Radar Anisotropy of Sea Ice Due to Preferred Azimuthal Orientation of the Horizontal C Axes of Ice Crystals: Journal of Geophysical Research**,** 83(C12), 6037-6046.

Matsuoka, K., T. Thorsteinsson, H. Bjornsson, and E.D. Waddington, 2007, Anisotropic radio-wave scattering from englacial water regimes, Mýrdalsjökull, Iceland, Journal of Glaciology, 53(182), 473-478.

Matsuoka, K., T. Furukawa, S. Fujita, H. Maeno, S. Uratsuka, R. Naruse, and O. Watanabe, 2003, Crystal-orientation fabrics within the Antarctic ice sheet revealed by a multi-polarization-plane and dual frequency radar survey, Journal of Geophysical Research, 108(B10), 2499.

Martinez, W.L., and A.R. Martinez, 2008, *Computational Statistics Handbook with MATLAB*, 767 pp., Chapman & Hall/CRC, Boca Raton, FL.

McGee, B.W., J. T. Harper, N. F. Humphrey, T. W. Pfeffer, 2003, Water Flow through Widespread and Interconnected Void Spaces at Depth in a Temperate Glacier: EOS (Trans., Amer. Geophys. Union), 84 (46), Abstract C11C-0850.

Meier, M. F., Dyurgerov, M. B., Rick, U. K., O'Neel, S., Pfeffer, W. T., Anderson, R. S., Anderson, S. P., and Glazovsky, A. F., 2007, Glaciers dominate eustatic sea-level rise in the 21st century: Science, 317: 1064–1067.

Meierbachtol, T., J. T. Harper, N. F. Humphrey, J. Shaha, and J. Bradford, 2008, Air Compression As A Mechanism For The Underdamped Slug Test Response In Fractured Glacier Ice: Journal of Geophysical Research Earth Surface, 113, F04009, doi:10.1029/2007JF000908.

Murray, T., A. Booth, D.M. Rippin, 2007, Water content of glacier-ice: Limitations on estimates from velocity analysis of surface ground penetrating radar surveys: Journal, Environ. Eng. Geophysics, 12(1) 87-99.

Murray, T., G.W. Stuart, M. Fry, N.H. Gamble, and M. D. Crabtree, 2000, Englacial water distribution in a temperate glacier from surface and borehole radar velocity analysis, Journal of Glaciology, 46(154) 389-398.

Navarro, F.J., Y.Y. Macheret and B. Benjumea, 2005, Application of radar and seismic methods for the investigation of temperate glaciers, Journal of Applied Geophysics 57(3) 193-211.

Nobes, D.C., 1999, The directional dependence of the ground penetrating radar response on the accumulation zones of temperate alpine glaciers: First Break, 17(7), 249-259.

Olhoeft, G.R., 2007, Adventures in Seeing the Unseen - from Borehole to the Moon, SAGEEP Proceedings, 323-331.

O'Neel, S., Pfeffer, W. T., Krimmel, R., and Meier, M., 2005, Evolving force balance at Columbia Glacier, Alaska, during its rapid retreat: Journal of Geophysical Research—Earth Surface, 110 (F3): F03012.

Patterson, W.S.B., 1994, *Physics of Glaciers*, 480 pp., Pergamon, Tarrytown, N.Y.

Petterson, R., P. Jansson and H. Blatter, 2004, Spatial variability in water content at the cold-temperate transition surface of the polythermal Storglaciaren, Sweden: Journal of Geophysical Research—Earth Surface 108:9.F02009.

Petterson, R., P. Jansson, and P. Holmlund, 2003, Cold surface layer thinning on Storglaciaren, Sweden, observed by repeated ground penetrating radar surveys: Journal of Geophysical Research, 109 F02009, doi: 10.1029/2003JF000110.

Pfeffer, W. T., J. T. Harper, and S. O'Neel, 2008, Kinematic Constraints on Glacier Contributions to 21st-Century Sea-Level Rise: Science 321, 1340-1343.

Sassen, D.S. and M.E. Everett, 2009, 3D polarimetric GPR coherency attributes and full-waveform inversion of transmission data for characterizing fractured rock: Geophysics, 74, J23, DOI:10.1190/1.3103253.

Schoenberg, M., and C.M. Sayers, 1995, Seismic anisotropy of fractured rock: Geophysics, 601), 204-0211.

Shen, F., X. Zhu, and M.N. Toksoz, 2002, Effects of fractures on NMO velocities and P-wave azimuthal AVO response: Geophysics, 67(3), 711-726.

Stern, A., 1929, Versuch einer elektrodynamischen Dickenmessung von Gletschereis, Ger. Beitr. Zur Geophysik, v. 23, p 292-333.

Taylor, L., 1965, Dielectric properties of mixtures: IEEE Transactions on Antennas and Propagation, 13(6), 943-947.

Thomas, R.H., Abdalati, W., Akins, T., Csatho, B., Frederick, E., Gogineni, S., Krabill, W., Manizade, S., Rignot, E., 2000, Substantial thinning of a major east Greenland outlet glacier: Geophysical Research Letters, 27 (9), 1291-1294.

Tsoflias G. P.**,** Van Gestel J. P., Stoffa P., Blankenship D. and M. Sen, 2004, Vertical Fracture Detection by Exploiting the Polarization Properties of GPR Signal: Geophysics, Vol. 69, No. 3, p. 803-810.

Tsvankin, I., and H.B. Lynn, 1999, Special section on azimuthal dependence of P-wave seismic signatures-Introduction: Geophysics, 64(4), 1139-1142.

Van Gestel, J.P. and P.L. Stoffa, 2001, Application of Alford rotation to ground-penetrating radar data: Geophysics 66, 1781, DOI:10.1190/1.1487120.

West, J.L., D.M. Rippin, T. Murray, H. M. Mader and B. Hubbard, 2007, Dielectric permittivity measurements on ice cores: implications for interpretation of radar to yield glacial unfrozen water content: J. Environmental Engineering Geophysics, 12(1), 37-45.

Wharton, R. P., et al., 1980, Electromagnetic propagation logging: advances in technique and interpretation, in 55th Annual Fall Technical Conference and Exhibition, Society of Petroleum Engineers, edited, p. 9267.

Yilmaz, O., 2001, *Seismic data analysis: processing, inversion an interpretation of seismic data. Second edition*, 2027 pp., Society of Exploration Geophysicists Tulsa, OK.

APPENDIX

Matlab Code Used to Generate Figures 10 and 12

Matlab Code Used to Generate Figures 10 and 12

```
%Equations and Plots from Taylor (1965)
%3/30/09*UPDATED ON 8/25/09...changing the orientation.
%Axis of disks is referencing axis of rotation.
clear all;close all;


%% Now plot resultant E using ice and water...varying the concentration
%from Taylor (1965)
ei=87;%water
eh=2.9154;%ice%from depth dep. mixing model with 0% total water .1% air
at surface.
z=0:.05:1;
%Disks
Eperp=eh.*(1-z)+z.*ei;
Epar=eh./(1+z.*(eh/ei-1));
Eran=ei.*((3*eh+2.*z.*(ei-eh))./(3*ei-z.*(ei-eh)));
%Spheres and Needles
x=(ei/eh);
Nb=(x-1-2.*z.*(x-1));
Nperp=eh.*((-Nb+sqrt((Nb.^2)+4*x))./2);

Sb=(x-2+3.*z.*(1-x));
Sphere=eh.*((-Sb+sqrt((Sb.^2)+8*x))./4);

Npb=(x-1+(5/3).*z-(5/3).*z.*x);
Npc=(-x+(1/3).*z.*x-(1/3).*z.*(x^2));
Nran=eh.*(-Npb+sqrt(Npb.^2-(4.*Npc)))./2;

figure(2)
hold on
plot(z, Eperp,'b');
plot(z, Epar,'r');
plot(z, Eran,'g');
plot(z, Nperp,'k');
plot(z, Sphere,'c');
plot(z, Nran,'m');
xlabel('Concentration Vi/Vt');
ylabel('Efffective Relative Permittivity')

%% Velocities
%Disks
vperp=.3./sqrt(Eperp);
vpar=.3./sqrt(Epar);
vran=.3./sqrt(Eran);
```

```
%Sphere and Needles
vnperp=.3./sqrt(Nperp);
vsphere=.3./sqrt(Sphere);
vnran=.3./sqrt(Nran);
figure(3)
hold on
plot(z, vperp,'b');
plot(z, vpar,'r');
plot(z, vran,'g');
plot(z, vnperp,'k');
plot(z,vnran,'m');
plot(z, vsphere,'c');

xlabel('Concentration Vi/Vt');
ylabel('Efffective Velocity (m/ns)')
legend('Disks Parallel (Needles Perpendicular)', 'Disks Perpendicular',
'Disks Random', 'Needles Parallel','Needles Random','Spheres')

%% Giordano
%Plot with varying allignment
%S=0:.25:1;%Order...0 =disorder 1=perfect order
%S(6)=.899;
S=[0 .4 .9 1]
con=0:.001:.2;%volume concentration of inclusions
for k=1:length(S)
    q=1-S(k);
    r=2+S(k);
    t=1+2*S(k);
    p=2-2*S(k);
    for j=1:length(con)
        gperp(k,j)=(q*ei*eh+r*(ei*eh+con(j)*(ei^2)-
con(j)*ei.*eh))/(q*(ei*(1-con(j))+con(j)*eh)+r*ei);
        gpar(k,j)=(t*ei*eh+p*(ei*eh+con(j)*(ei^2)-
con(j)*ei.*eh))/(t*(ei*(1-con(j))+con(j)*eh)+p*ei);
    end
end
vgpar=.3./sqrt(gpar);
vgperp=.3./sqrt(gperp);
figure(4)
hold
plot(con,vgperp(1,:),'g')
plot(con,vgpar(1,:),'g--')
plot(con,vgperp(2,:),'b')
plot(con,vgpar(2,:),'b--')
plot(con,vgperp(3,:),'r')
plot(con,vgpar(3,:),'r--')
plot(con,vgperp(4,:),'k')
plot(con,vgpar(4,:),'k--')
%plot(con,vgperp(5,:),'m')
%plot(con,vgpar(5,:),'m--')
% plot(con,vgperp(6,:),'k')
% plot(con,vgpar(6,:),'k--')
xlabel('Concentration Vi/Vt');
ylabel('Efffective Velocity (m/ns)')
```

```
legend('Parallel S=0', 'Perpendicular S=0', 'Parallel S=0.4',
'Perpendicular S=0.4','Parallel S=0.9', 'Perpendicular S=0.9','Parallel
S=1', 'Perpendicular S=1')


h=findobj('Type','Text');
linobj=findobj('Type','line');
set(linobj,'LineWidth',2);
set(h, 'fontunits', 'points');
set(h,'fontsize',18);
%set(h, 'fontweight', 'bold');
```